Bottom water hydrodynamic provinces and transport patterns of the northern South China Sea: Evidence from grain size of the terrigenous sediments

Author names and affiliations

Yi Zhong, Key Laboratory of Marginal Sea Geology, South China Sea Institute of Oceanology, Chinese Academy of Sciences, Guangzhou 510301, China

Tel: +86-20-89021046(o); Mob: +86-15602335786, Email: zhongyi@scsio.ac.cn

Zhong Chen, Key Laboratory of Marginal Sea Geology, South China Sea Institute of Oceanology, Chinese Academy of Sciences, Guangzhou 510301, China

Tel: +86-20-89023149(o); Mob: +86-13610001305, Email: chzhsouth@scsio.ac.cn

Liang Li, Marine Geology Survey Institute of Hainan Province, Haikou 570206, China

Tel: +86-20-66567278(o); Mob: +86-15348884237, Email: brighting_lee@163.com

Jianguo Liu, Key Laboratory of Marginal Sea Geology, South China Sea Institute of Oceanology, Chinese Academy of Sciences, Guangzhou 510301, China

Tel: +86-20-89024537(o); Mob: +86-13826454085, Email: jgliu@scsio.ac.cn

Gang Li, Key Laboratory of Marginal Sea Geology, South China Sea Institute of Oceanology, Chinese Academy of Sciences, Guangzhou 510301, China

Tel: +86-20-89022579(o); Mob: +86-13570278774, Email: gangli@scsio.ac.cn;

Xufeng Zheng, Key Laboratory of Marginal Sea Geology, South China Sea Institute of Oceanology, Chinese Academy of Sciences, Guangzhou 510301, China

Tel: +86-20-89021046(o); Mob: +86-15521098650, Email: zxf@scsio.ac.cn;

Shuhong Wang, Key Laboratory of Marginal Sea Geology, South China Sea Institute of Oceanology, Chinese Academy of Sciences, Guangzhou 510301, China

Tel: +86-20-89021046(o); Mob: +86-13533484970, Email: wshds@scsio.ac.cn;

Aibin Mo, Key Laboratory of Marginal Sea Geology, South China Sea Institute of Oceanology, Chinese Academy of Sciences, Guangzhou 510301, China

Tel: +86-20-89023861(o); Mob: +86-15625043997, Email: abmo@scsio.ac.cn

*Corresponding author: Zhong Chen, chzhsouth@scsio.ac.cn

Bottom water hydrodynamic provinces and transport patterns of the northern South China Sea: Evidence from grain size of the terrigenous sediments

Yi Zhong [a,b], Zhong Chen [a,*], Liang Li [c], Jianguo Liu [a], Gang Li [a], Xufeng Zheng [a],
Shuhong Wang [a], Aibin Mo [a,b]

[a] CAS Key Laboratory of Marginal Sea Geology, South China Sea Institute of Oceanology, Chinese Academy of Sciences, Guangzhou 510301, China

[b] University of Chinese Academy of Sciences, Beijing 100049, China

[c] Marine Geology Survey Institute of Hainan Province, Haikou 570206, China

*Corresponding author: chzhsouth@scsio.ac.cn

Abstract: Sediment transport in the source-to-sink systems of the northern South China Sea (SCS) has been of increasing interest during the past few decades. However, the mechanisms for sediment redistribution remain unclear. Sources and transport patterns in the northern SCS were investigated in this study based on grain size analyses of 205 surface sediment samples. Detailed characterizations of hydrodynamic conditions and sediment transport have been made using the log-ratio method to partition grain size components of surface sediments in the northern SCS. Results reveal that sediment dispersal patterns in the region generally contain traction, saltation, graded and uniform suspension modes. Based on the spatial distribution characteristics, the study area can be classified into three hydrodynamic provinces. Province A contains high traction concentrations that are exposed to the longshore current and topographic features, which are distributed in the Taiwan Shoal, Dongsha Islands and extends from the Pearl River estuary to the southeast of Hainan Island. Province B is characterized by higher values of saltation and graded suspension, which are widespread along the northern slope of the SCS, and its formation is interpreted as the result of interactions between down- and along-slope processes. Province C reaches its greatest concentration in the abyssal areas, particularly in the vicinity of Luzon Island, which settles only under calm conditions. Combined with previous data concerning magnetic susceptibility distributions of surface sediments from the northern SCS, the sediment transport route near the mainland is traced. Furthermore, based on distribution pattern of sortable silts and hydrodynamic provenance of the terrigenous sediments, the sediment transport route in the deep water region of the northern SCS is outlined. It flows along marginal channels which cut across the continental slope along isobaths. Taken together, the combination of grain-size components and sortable silts of surface sediment used here is a promising tool to better assess the modern variability of hydrodynamic conditions and transport processes in marine environments.

Keywords: Grain size distribution; Sortable silt; Mathematical partitioning; Sediment transport; Hydrodynamic conditions; Northern South China Sea

1. Introduction

The South China Sea (SCS) is an excellent case setting for the study of sediment source-to-sink transport process, especially for enclosed or semi-enclosed systems during sea level lowstands, in which case the sediment transport pathways can be more easily defined (Liu et al., 2016). As the largest of the marginal seas separating Asia from the western Pacific, the northern SCS has a special attraction for marine geologists because of the very high sedimentation rate of its detrital sediments (Wang and Li, 2009). The northern SCS is an area of active sedimentation with possible input of terrigenous sediment from the Pearl, Red and Yangtze rivers, as well as the islands of Taiwan and Luzon (Shao et al., 2009; Wan et al., 2007). After these river-derived terrigenous sediments enter the sea, most are deposited on the continental shelf, but a small amount is transported further where it is deposited on the abyssal basin (Liu et al., 2011). Regardless, sediment transport and depositional dynamics involve ocean circulation, which is comparatively complex in the SCS (Wan et al., 2010). Surface currents in the SCS are driven by southwestern winds in summer and northeastern winds in winter (Fernando et al., 2007; Hu et al., 2000b). The dynamic processes driven by downslope and along-slope currents play a significant role in constructing and shaping continental margins (Chen et al., 2014).

In recent years, a number of sedimentological and geochemical approaches, including measurements of grain size distribution (Huang et al., 2011; Li et al., 2011;

Wan et al., 2007) and the occurrence of clay and heavy minerals (e.g., Liu et al., 2012; Liu et al., 2008b; Li et al., 2015, 2016; Zhong et al., 2017), as well as strontium and neodymium isotopes (e.g., Shao et al., 2009; Wei et al., 2012; Huang et al., 2014) and major and trace element geochemical properties (Cai et al., 2013; Liu et al., 2010c, 2013) of surface and core sediments in the northern SCS have been suggested as proxies that are capable of constraining sources and transport pathways, as well as to elucidating related paleoenvironmental and paleoclimatic information (Liu et al., 2012; Liu et al., 2010c; Liu et al., 2015). Nevertheless, many previous suggestions and proxies for sediment provenance in this area are not coincident and are sometimes even controversial. What is more, the transport mechanisms of detrital terrigenous sediments from various source areas in the northern SCS and conditions related to their depositional hydrodynamics are less understood.

Grain size components were related to sources of hydrodynamic conditions in marine sediments (Carranza-Edwards et al., 2005; McCave, 1978; Nordstrom, 1981; Self, 1977; Visher, 1969). Sediment grain size is usually applied to studies of sedimentary environment, depositional processes, and material sources, which can also be used to infer the mode of sediment transport as an important indication of environmental impact (Christiansen et al., 1984; Ghoshal et al., 2010; Miousse et al., 2003; Purkait, 2006; Wang et al., 2003). Therefore, several approaches have been employed to correlate variations in sediment grain size with the hydrodynamic conditions that control sediment transport. The introduction of multivariate statistical and statistical analysis methods has led to the realization of the environmental significance of polymodal sediments and related cumulative log probability curves to specific environments (Folk and Ward, 1957). Some studies of grain size subsequently have focused on establishing links between sedimentary environments and the summary statistics of grain size distributions (GSDs), such as the mean, standard deviation (sorting), skewness and kurtosis (Folk and Ward, 1957; Friedman, 1979; Shepard, 1954). Boulay et al. (2003) extracted “components” that are sensitive to environmental conditions based on measured relationships between mean grain size and standard deviation. Other studies have suggested a more dynamic concept in which spatial patterns of summary statistics were assumed to reflect net sediment transport pathways (Gao et al., 1994; Le Roux and Rojas, 2007). Moreover, each log-normal sub-population may be related to a different mode of sediment transport and deposition, thus providing a quantitative measurement of importance in the genesis of sediment dynamics (Visher, 1969). In this study, the characteristics of sea-bottom sediment grain size have been evaluated by log-ratio analysis to gain a better understanding of sediment dynamics in the northern SCS.

The grain-size characteristics of current deposits have been proposed as an estimate of the strength of abyssal flow (Ellwood and Ledbetter, 1977). McCave et al. (1995) put forward a more specific grain-size proxy, which is more sensitive to the variation of flow strength. The terrigenous silt fraction in the 10–63 μm range was termed sortable silt (SS), and the abundance of this fraction varies with current intensity. Although the proxy of SS has been widely used around the world (Ellison et al., 2006; Kissel et al., 2010; Negre et al., 2010), there have been limited analyses on the transport trend based on the sortable silt of bottom sediments from the northern SCS.

The objectives of this paper are to unravel the depositional dynamic conditions and sediment transport system in the northern SCS. We first address hydrodynamic partitioning by a log-normal sub-population of grain size. Then the influencing factors of different sources are analyzed at various locations in the northern SCS. Finally, their transport routes are explored by the sortable silts of terrigenous sediment sources in the entire northern SCS.

2. Regional setting

2.1. Geological and oceanographic settings

The SCS is one of the largest marginal seas in the western Pacific. It is bounded by the Indochina Peninsula to the west, by southern China to the north, by the Philippine arc to the east, and by Malaysia and Indonesia to the south (Wang and Li, 2009) (Fig. 1a). The SCS, with an area of 3.5×10^6 km^2 and water depths in excess of 5000 m, extends to the northeast (Zhu et al., 2010). Its seafloor topography is very complex and widely variable, with several plateaus, troughs, valleys and island reefs. The study area (17.5°–24°N and 109°–121°E) has a broad continental shelf (depths shallower than 200 m) and a large deep basin (with the maximum depth greater than 4000 m) (Fig. 1b). This area is strongly dissected by deep-marine erosive channels, submarine canyons, and slope gullies, all of which act as active conduits for the delivery of clastic sediments from the SCS shelf and upper slope into the deep-marine environment (Chiu and Liu, 2008; Gong et al., 2015).

Modern oceanic circulation in the SCS is influenced mainly by the semi-enclosed-basin physiography, the main oceanic water masses, and atmospheric circulation (Qu et al., 2006; Zhu et al., 2010). It preserves water exchange through straits with the Pacific Ocean, Indian Ocean, and the adjacent marginal seas. There are various water masses at different water depths in the SCS (Fig. 1b). The overall surface current circulation of the SCS is dominantly cyclonic (counter-clock-wise) in winter and anti-cyclonic (clockwise) in summer, driven by seasonal monsoons (Fang et al., 1998; Shaw and Chao, 1994; Wan et al., 2010; Wyrtki, 1961; Xue et al., 2004). The oceanic circulation over the continental shelf in the northern SCS is also heavily impacted by the wind forcing, the Kuroshio intrusion, and mesoscale processes (Fang et al., 2015; Qu et al., 2004; Zhang et al., 2006). The Kuroshio Current intrudes into the northern SCS and transports the upper 300–500 m of water westward along the northern continental slope of the SCS (Liu et al., 2011; Shaw and Chao, 1994). A series of mesoscale anticyclonic eddies distributed along the continental slope from the southwest of Taiwan to the west of Dongsha Islands (referred to as the Loop Current and SCS Branch of Kuroshio/SCS Warm Current, respectively) were suggested as the detachment of warm rings from the Kuroshio (Caruso et al., 2006; Hu et al., 2000a; Yuan et al., 2006). The SCS Warm Current is a northeastward flow separated from the SCS Branch of the Kuroshio Current. The Guangdong Coastal Current flows northwest and is largely controlled by the winter monsoon. In summer, the SCS Branch of the Kuroshio Current also shifts southeast and the Guangdong Coastal Current is reversed, while the SCS Warm Current becomes the prevailing northeasterly surface current forced by summer monsoon winds (Qu et al., 2009).

Besides, there exists a deep water current (2000–2500 m) that turns southwest along the continental margin off the southeast China coast called the SCS Contour Current (Qu et al., 2006; Tian et al., 2006; Wang et al., 2011; Zhao et al., 2014). The Luzon Strait with a sill depth of about 2400 m is the only deep passage connecting the SCS with the western Pacific (Wang and Li, 2009; Li and Gong, 2016). Influenced by the southwestward intrusion of the NPDW through the Luzon Strait, the average bottom current velocity exceeds 0.15 m/s at water depths of 2500 to 2600 m in the Bashi Channel, with maximum velocities reaching 0.3 m/s (Xie et al., 2009a, b) (Fig. 1a). As the NPDW flows along the northern margin of the SCS, a series of NE-and WSW-oriented migrational channels have developed in the northern slope of the SCS (He et al., 2013; Li et al., 2013).

2.2. Source regions

The terrigenous input derived from large rivers is greater than that from eolian particles transported from mainland China or volcanic ashes from the Philippines and Indonesia (Chung et al., 2004). At Ocean Drilling Program (ODP) Site 1146, only ~10% of the total clay and ~10% of the terrigenous fractions are related to eolian supplies (Boulay et al., 2007; Wan et al., 2007). A study of the inner shelf of the East China Sea also revealed that the Yangtze River (loading of 470 Mt/a) (Milliman and Farnsworth, 2011) does not supply significant sediment to the SCS through the Taiwan Strait (Xu et al., 2009). As a result, in the northern SCS, predominant sediment sources include the Pearl River, southwestern Taiwan and the Luzon arc system (Fig. 1b) (Liu et al., 2010c; Liu et al., 2008b), which annually deliver a substantial amount of terrestrial sediment to the northern SCS, making it as a significant sediment sink.

Among these fluvial drainage systems, Pearl River sediment discharge (~80 Mt/a) is mostly transported southwestward where these sediments are largely deposited on the inner shelf (Ge et al., 2014; Liu et al., 2011; Liu et al., 2014). Luzon sourced sediments (~11 Mt/a) are generally deposited to the northwest of Luzon and are not significantly transported onto the northern shelf by the branch of the Kuroshio Current

(Liu et al., 2011; Liu et al., 2009b). In contrast, southwestern Taiwan supplies large amounts of sediments (~70 Mt/a) into the northeastern SCS via small mountainous rivers (e.g., the Kaoping River) (Liu et al., 2008a). Meanwhile, Hainan Island, the second largest island in China, is a continental-type island in the northern SCS from which a low sediment flux (~4 Mt/a) is consistent with low mass accumulation rates on the neighboring shelf (Hu et al., 2014; Wang, 1999) (Fig. 1b).

3. Materials and methods

3.1. Sample collection

A large number of unevenly distributed surface sediment samples (upper 5 cm of the seafloor) from the northern SCS were collected using box or grab samplers by the South China Sea Institute of Oceanology (SCSIO) of the Chinese Academy of Sciences (CAS) during the past 10 years. The 205 sample stations in the northern SCS are shown in Fig. 2 and Table 1. The distribution of sample locations was devised to collect material from a broad range of hydrodynamic depositional environments. In this paper, 131 samples were obtained from continental shelf sites, 40 samples were located at on the continental slope, and other samples were deposited evenly in the deep-sea basin within the study area.

3.2. Analytical methods

3.2.1. Grain-size measurements

The sediments deposited in the northern SCS originate from all the surrounding regions. They are first transported by rivers flowing on the southeastern side of Asian continent and on the various bordering the southern and eastern sides of the SCS before being taken up by the different oceanic water masses and progressively deposited at sea (Liu et al., 2016). Marine sediments include terrigenous, biogenic, volcanogenic, cosmogenic and authigenic components, relationship between which depend on specific facies environments (Sval'nov and Alekseeva, 2006). In order to better use the composition of the marine terrigenous fraction as a tracer of hydrodynamic conditions, it is first critical to isolate the terrigenous fraction of these sediments by the chemical extractions.

Grain-size distributions of the terrigenous sediment fraction were determined by laser particle sizing after chemical removal of organic carbon, calcium carbonate ($CaCO_3$), Fe-Mn authigenic minerals and biogenic opal (Clemens and Prell, 1990; Hovan, 1995; Rea and Janecek, 1981). About 200 mg of sediment from each air-dried, disaggregated sample was pretreated with 10–20 mL of H_2O_2 (30%$_{v/v}$) to remove organic matter, then with 10 mL of 10% HCl (15%$_{v/v}$) with the sample solution boiled to remove carbonates. About 2000 mL of deionized water were added, and the sample solution was kept for 24 h to rinse acidic ions. The residues were further treated with excess 0.3 M $Na_3C_6H_5O_7$, 1 M $NaHCO_3$ and a bit of $Na_2S_2O_2$ to remove Fe-Mn oxides, then excess 2 M Na_2CO_3 with the sample solution boiled to remove biogenic opal. Between every chemical reaction, samples were washed with demineralized water. To avoid clay-mineral aggregation, 10 mL of 0.05 M $(NaPO_3)_6$ were added to the sediment solutions before analysis and by ultrasonic treatment for 10 minutes before measurement.

The analyses were performed using a laser particle sizer (Malvern Mastersizer2000) in the SCSIO. As the range of grain size measurement was 0.02–2000 μm，at 1 φ intervals, the samples were separated into two parts according to the grain size. Samples within this range were measured directly, whereas coarse particles (>2000 μm) were sieved with a sieve mesh of 1 mm. The part over the sieve was analyzed with standard sieving methods, and the part below the sieve was measured directly, then the two parts data were combined using the simulated program of Mastersizers2000 to get the whole grain size. Analyses were performed in triplicate on each sample, the mean values of each parameter were calculated and the associated standard deviations were <3%.

3.2.2. Partitioning of grain-size components

The identification of hydrodynamic partitions is an important part of this research in the northern SCS. To interpret the genesis of each grain-size component within an individual polymodal distribution and to relate the constituent grain-size components to specific depositional processes and sedimentary environments, sedimentologists have made substantial efforts to define different types of grain size distributions and partition the constituent components of ploymodal sediments with the aid of mathematical methods (Chen et al., 2013a; Sun et al., 2002; Xiao et al., 2009; Xiao et al., 2013; Yi et al., 2012). In this study, we use log-ratio methods to analyze the relationships between the sedimentary components of the samples, which represent the different hydrodynamic modes of the sea-bottom sediments.

Analysis based on log-probability distributions of sediment grain sizes has suggested that each log-probability sub-population may be related to a different mode of sediment transport processes (surface creep or rolling/traction, saltation and suspension) (Visher, 1969), thus providing a measure of their importance in the genesis of grain-size components. These transportation modes respectively represent the traction component, the saltation component and the suspension component. Moreover, the intercept point between the line segments of the suspension component and the saltation component is called the *fine intercept point*. The intercept point between the line segments of the saltation component and the traction component is called the *coarse intercept point*. The fine intercept point represents the maximum grain size of the suspension component. Generally, the smaller the fine intercept point is, the stronger the hydrodynamic energy is. In contrast, the larger the fine intercept point is, the weaker the hydrodynamic energy is (Folk, 1966; Folk and Ward, 1957). Sensitive grain size components are the components that are sensitive to the hydrodynamic energy of a specific depositional environment. Therefore, they can be used to indicate the different hydrodynamic conditions with specific amounts of hydrodynamic energy. Based on the above-mentioned log-probability analyses for the northern SCS samples, combined with historical records of other recorded literatures, we can infer the hydrodynamic volumes of northern SCS terrigenous sediments.

4. Results

4.1. Grain size composition and distribution

Given that grain-size components in sea bottom sediments reflect different transportation or depositional processes and preserve environmental information about these processes (Yi et al., 2012), it is clearly desirable to be able to separate out specific components in terrigenous samples. Grain sizes in terrigenous sediments are controlled jointly by sediment provenance, hydrodynamic conditions, topography and other factors of the sedimentary area. Therefore, the grain size potentially can be used to identify different sources supplying sediment from mainland and dynamic depositional environments.

The terrigenous sediments of the northern SCS are composed of gravel (5–38%, average 20%), sand (0–97%, average 32%), silt (1–78%, average 46%) and clay (0–54%, average 21%). The skewness range, kurtosis values and sorting coefficient are –0.85 to 0.33, 0.60 to 8.02, and 0.35 to 3.87 with average values of –0.19, 1.16 and 2.09, respectively. The spatial distributions of these granular contents are shown in Fig. 3. In the northern SCS, the gravel content is mainly transported out of Taiwan Shoal, then deposited in the Pearl River Delta and offshore from Hainan Island (Fig. 3a). The high sand percentage (>60%) is primarily deposited on Taiwan Shoal and southward along the continual shelf in the study area (Fig. 3b). The silt content is the dominant component in the study area, with high levels (>60%) widely distributed in the offshore, continental shelf, continental slope and deep sea (Fig. 3c). The clay values display a trend that extends to the lower continental slope and deep-sea basin (Fig. 3d).

The spatial distribution of the medium diameter of the sea-bottom sediments shows a clear coarse-fine trend from the nearshore to the open sea. On average, the diameter of sediments on the sea-bottom in the northern SCS averages 5.27 φ, and they show wide spatial variation, ranging from –0.42 φ to 8.12 φ [where, φ = –log2 (diameter in mm)]. Data presented in Fig. 4 indicate that changes in median grain size are controlled by water depth and there is a big difference between shallow and deep water. The median diameter of sea-bottom sediment on the continental shelf (water depth <200 m) is more variable and reflects the feedback between morphology and sediment exchange. The limited median diameter variation of sea-bottom sediment over a wide range of deeper water depths. The coarsest sea-bottom sediments in the three main districts are present by those on the shelf of the SCS, while the finest are present on the slope and in the deep ocean. Fine-grained sediments increase in fraction on the continental slope (water depths 200–2000 m) to over 60%. Furthermore, in the abyssal basin (water depths >2000 m), sediments are mostly fine-grained with some coarse-grained material. In this study, only two samples had a more coarse-grained fraction in the deep-water area (water depth >200 m). Therefore, the topographic influence on grain sizes of terrigenous sediments should be obvious when investigating sediment provenance and depositional processes.

4.2. Characteristics of grain-size components

The cumulative probability curves of Visher (1969) produce characteristic grain-size distribution plots that reveal coarse and fine truncation points and specific ranges for the percentage distribution of populations of particles transported by traction, saltation and suspension. This approach has been used successfully to analyze sands from several modern environments, such as dunes, beaches, rivers, deltas, tidal channels, and turbidity currents (Luo et al., 2013). In addition to the hydrodynamic characteristics of nearshore regions, there are various depths and complex terrains in the northern SCS. So hydrodynamic partition in the surface sediments of the northern SCS mainly consist of traction (17–100%, average 41%), saltation (0–67%, average 26%), graded suspension (10–85%, average 32%) and uniform suspension (11–34%, average 24%) (Fig. 5). Furthermore, Fig. 5 shows the results of GSD and the log-probability cumulative curves for the studied samples in the northern SCS. These results illustrates that differently sized subpopulations are mixed in these sediments.

Traction content in the northern SCS is mainly distributed on the continental shelf. There are two major areas with high traction contents (>40%), the first being adjacent to the Taiwan shoal and the second being the northeastern Dongsha Islands. Another high traction area extends to the shelf and even the slope between the Pearl River mouth and eastern Hainan Island (Fig. 5a). For samples from high traction content areas (sites 04E604 and 79-7), the curves have two types of segments, including one and four segment modes. For example, the GSD of site 04E604 shows a normal distribution, and the data indicate a well-developed traction population, comprising all of the grains, and indicating coarse grain size. In contrast, the 79-7 sample has a high traction population (55.1%), low saltation (9.6%) and two types of suspension (19.2% and 16.1%, respectively) with a similar normal distribution. Clear coarse and fine truncation points occurred at 1.1 φ and 1.8 φ, respectively.

In addition, areas of high saltation content (>40%) and graded suspension (>35%) are mainly distributed on the continental slope (Fig. 5b-c). Each size distribution is plotted in an identical fashion, and all show different subpopulations. The probability cumulative curves for the high saltation value area show a three-segment mode. Site 09E109 has a normal distribution and a high saltation population (60.5%), low graded suspension (14.6%) and moderate uniform suspension (24.8%). The coarse truncation point occurs at 4.6 φ. The probability cumulative curves for the high graded suspension value areas show two kinds of modes: a four-segment mode and a two-segment mode. The former mode (site 09E401) consists of two suspension components (48.9% and 20.5%), a jumping component (1.4%) and a rolling component (29.2%). The coarse intercept point is 1.5 φ and fine intercept point is 4.4 φ. The latter mode (site 79-54) consists of two suspension components including graded (79.7%) and uniform (20.3%) suspension.

In contrast, high suspension content (>25%) was found mainly adjacent to the Luzon Islands in abyssal basins (Fig. 5d). The sample (site 11E109) from the high suspension area is composed of saltation (28.5%) and two suspension fractions (42.0% and 29.5%) which is truncated at about 5.3 φ.

5. Discussion

5.1. Sediment hydrodynamic provinces

The spatial distribution of sediment dynamics in the northern SCS can provide a macro-scale view of the source-to-sink transport of terrigenous sediments on time scales of years to tens of years. However, the lack of effective proxies and systemic analyses precludes detailed interpretations of the distribution and provenance of these sediments hydrodynamic sediments. To better evaluate the dominant transport processes based on these recently deposited surface sediments, a comprehensive comparison of sediment hydrodynamics with various current systems in the northern SCS is needed. Based on the spatial distribution of the four major dynamic partition compositions, we divide the basin-wide area into three provinces (A, B and C) that display distinct assemblages of hydrodynamics.

5.1.1. Province A

The Province A comprises the medium to coarse sand size range (−1 to 2 φ). It is sufficiently large that it may represent intermittent bed load transported during high-energy currents or under storm conditions. It is characteristic of high traction content (total ~45%) with minor saltation and suspension, which can be divided into three traction partition content areas (named A1-A3). Area A1 lies around the Taiwan Shoal, mainly controlled by local topography and local currents. The Taiwan Shoal is a tectonically raised platform that has been rebuilt by storm waves and strong winds in previous glacial and interglacial periods (Yu and Song, 2000). Liu and Xia (2004) proposed that the Taiwan Shoal not only consists of relict deposits but also modern deposits. The sandwaves there are subjected to the action of tidal currents and typhoon currents. The size and shape of sandwaves are proposed to have been controlled by current velocity, sediment particle size, and water depth (Du et al., 2010). In addition to its terrain fluctuation, the Taiwan Shoal was strongly influenced by Pacific low-pressure cyclones and SCS cyclones, and the local hydrodynamics are controlled by SCS flow, the Hanjiang River, a branch of Kuroshio Current, and upwelling.

Area A2 lies in the western Dongsha Islands, extending from the lower slope to the outer shelf. The area fits within a region of flow direction change from the westward SCS Branch to the Kuroshio and SCS Warm Current. The SCS Branch of Kuroshio and SCS Warm Current exist in both winter and summer, regardless of any change of monsoon winds (Fang et al., 1998; Liu et al., 2013). In this case, they compose a series of mesoscale anticyclonic eddies distributed along the continental slope from southwestern Taiwan to the western Dongsha Islands. Because of the strong erosion of surface sediment since the tectonic uplift of Dongsha, there are almost no modern sediments on the middle and outer shelves in the Dongsha area (Lüdmann and Wang, 2001; Li et al., 2008; Lüdmann and Wong, 1999; Yan et al., 2006). Sand materials in the study area mainly originate from the erosion of the bed sediment formation. Moreover, very large subaqueous sand dunes were discovered on the upper continental slope of the northern SCS (Reeder et al., 2011). Therefore, the high traction content in the western Dongsha Islands seems to be transported mainly by the surface current under the influence of the Kuroshio intrusion.

Area A3 in the northern SCS has a distinct tongue-shaped pattern extending from the Pearl River estuary to southeastern Hainan Island. The distribution of high traction values mostly can be coupled with local surface current water and river input. The Pearl River drains through South China where the western region is dominated by Paleozoic-Mesozoic carbonate rocks and the east mainly consists of Mesozoic-Cenozoic granitic rocks and Paleozoic sedimentary rocks (limestone, shale and sandstone) (Liu et al., 2007). Recent work has indicated that the Pearl River has formed a 400-km-long elongated shore-parallel Holocene mud deposit, extending from the Pearl River delta to the southwest off the Guangdong coast to the Leizhou Peninsula (Ge et al., 2014; Liu et al., 2014). During the summer, the Pearl River sediments entering the estuary are mostly trapped within the shelf area near the estuary. The westward Guangdong Coastal Current during the winter along with the longshore current should have resuspended and reworked any deposited sediments (Ge et al., 2014; Liu et al., 2014). However, the high traction contents near the southeast part of Hainan Island are most likely sourced from the small rivers on Hainan Island, which can be associated with terrigenous input from the Wanquan and Nandujiang rivers (Zhang et al., 2013). This probably indicates the dispersal pathway of the Hainan sediments, transported by the northeastward flowing SCS Warm Current.

5.1.2. Province B

In the northern SCS, the surface sediments from the continental slope consist of dynamic interaction currents, representing two different transport conditions and presumably producing two separate populations of saltation and graded suspension in different flow directions (Stow, 2009). The relationships of fractions in deep-water sediments are influenced by the sediment supply, morphology, slope gradient, tectonic movement and so on (e.g., Antobreh and Krastel, 2006; Cunningham et al., 2005; Shepard and Emery, 1973). Province B is interpreted as a scour zone that includes higher saltation and graded suspension populations with minor traction and uniform suspension, which are considered evidence of significant deep water current transportation in the northern SCS (Fig. 6).

In the previous study, the geometries, morphology, and internal seismic reflection configurations confirmed giant elongated, confined, and slope sheeted drifts, as well as sediment waves are widespread in the northern slope (Li et al., 2013). Combined with content distribution and cumulative frequency plots (Fig. 5b and 5c), Province B is mostly defined by the sand and silt (2 to 5 φ) size range, which is widespread on the northern slope of South China Sea, and the formation of high saltation and graded suspension areas is interpreted as the result of the interactions between down- and along-slope processes. Grain size distribution patterns of both the sandy and silty facies are mostly fine- to medium-grained, sharing significant similarities to those observed in many other contourites (Stow et al., 2008). In this case, bottom current deposits are usually classified as mid-water bottom current deposits between 300 and 2000 m and deep-water bottom current deposits in water depths exceeding 2000 m (Stow et al., 2002). And most bottom current deposits are elongated sub-parallel to the continental margins. Especially, large-scale undulating bedforms found upon the lower slope of the SCS Slope off southwestern Taiwan at water depths of 300–3200 m are interpreted to be sediment waves (Gong et al., 2012). Furthermore, the integrated data and the depositional model show that the upper slope of the study area is strongly dissected and eroded by down-slope gravity flows. Sediments shed from the upper slope and transported basinward into the lower slope where interactions of down-slope turbidity currents and along-slope bottom (contour) current induced by the intrusion of the Northern Pacific Deep Water into the study area (Gong et al., 2012; Kuang et al., 2014; Zhong et al., 2015). Through erosion, transport and deposition of sediments, such dynamic processes can generate complex deep-water sedimentary systems, including turbidites, mass-wasting sand contourites (Chen et al., 2013b). For example, deep-water contour currents may circulate counterclockwise and be transported northeastward through Dongsha Islands to Xisha Island, bifurcating in the Xiasha Islands because of topographical prominences (Li et al., 2013). As discussed above, the deposition of the studied sediment is controlled by the interactions between down- and along-slope processes with the seafloor morphology.

5.1.3. Province C

Province C shows higher suspended content with a modal size <4 μm in the fine clay size range. It is likely to represent uniform suspended load in the marine environment, which settles only under calm conditions. Once settled, the load is difficult to move because of the cohesive properties of the clay-sized particles. The spatial pattern of Province C reaches its greatest concentration in the abyssal areas, particularly in the vicinity of Luzon Island, suggesting that it is supplied by volcanic sources.

5.2. Sediment transport patterns

Previous sedimentological investigations from the northern SCS are included here to provide regional context for the source-to-sink studies. For example, such studies include sediment transport in the Kaoping River Canyon systems in the northern SCS (Liu et al., 2009a), sediment flux and transport in the Taiwan Strait (Liu et al., 2008b), transport of clay mineral species in the northeastern South China Sea, terrigenous supply from Taiwan to the northern South China Sea (Liu et al., 2010c; Liu et al., 2008b). Unfortunately, not much work has been undertaken on sediment transport patterns in the northern SCS, although they are equally as important as analyses of tectonics and structures both in terms of academic interests and petroleum exploration. Regardless of which methods have been employed for determining sediment transport, one of the most direct and obvious pieces of evidence in support of sediment migration is that some fractions increase or decrease significantly in the direction of sediment transport. Herein, through mathematical decomposition, content changes of each sub-population have been estimated. These estimates can be used to detect and evaluate the sediment transport mechanisms.

5.2.1. Sediment transport in the nearshore

The general surface circulation in the SCS changes largely on a seasonally basis with monsoon wind. It is also strongly influenced by the intrusion of the Kuroshio Current into the northern part of the SCS (Chen and Wang, 1998; Dongliang, 2002). According to the traction content distribution, high traction sediments from the Taiwan Shoal and Dongsha Islands are controlled by both Kuroshio intrusion into the SCS and the China coastal current. High traction sediments from the Pearl River and Hainan Island are transported southwestward under the coastal current in winter and ultimately are mostly deposited between the Pearl River mouth and Hainan Island. The main sediment provenances and the currents which could transport terrestrial material in the northern SCS are summarized in Fig. 9. The direction could reveal the source-to-sink course well in these three provinces, which is consistent with the hydrodynamic setting.

Several studies have demonstrated that the magnetic properties of sediments are sensitive to bulk sediment particle size, which in turn is strongly influenced by hydrodynamics (Liu et al., 2010b; Oldfield et al., 2009; Oldfield and Yu, 1994; Zhang and Yu, 2003). Furthermore, sediment source determinations and their distribution based on the magnetic susceptibility (MS) of surface sediments can also confirm the hydrodynamic conditions in the northern SCS (Liu et al., 2010a). Fig. 7 shows sediment sources and their relationship with surface circulation in the northern SCS, based on high MS values of surface sediments and provides an effective means to track detrital sediment dispersal patterns (Ellwood et al., 2006).

In these source areas, sediment deposits containing a large fraction of high-coercivity magnetic minerals, such as the ilmenite, rutile, magnetite, zircon, monazite, and xenotime (Li et al., 2015), could have been initially discharged from major river systems in China and deposited in nearshore environments around the Pearl River mouth and Hainan Islands. Turbulent mixing, as one of the most important dynamic characteristics of these estuary and near-shore waters, plays a vital role in the dispersal of terrestrial water enriched with metallic element and sediments. They are mainly generated by bottom stress, internal shear instability, and wind effects (Pan and Gu, 2016). After current sorting, selective fine grained sediments, including fine-grained high-coercivity magnetic minerals, were probably transported to the northwestern shelf of the South China by the China coastal current and South China Sea Warm Current (Dong et al., 2004), as already revealed by mineral assemblage investigations (Chen et al., 1986; Zhong et al., 2017). In addition, to the west of Luzon Island, sediments with the highest MS values are transported northwestward predominantly under the influence of Kuroshio intrusion, which brings warm and salty waters from the western Pacific into the SCS through the Luzon Strait (Liang et al., 2003; Wu and Chiang, 2007). The high MS values in samples from the western Luzon islands reflect the contribution of Luzon island volcanic source materials, and these sediments are subsequently deposited along the route of the Kuroshio intrusion. For another, the spatial distribution of illite + chlorite contents in the northern SCS displays a double tongue-shaped pattern extending from offshore Taiwan to the southwest along the ~100 m contour and from southeastern Hainan northeastwards along the continental slope (100–200 m isobaths), which corresponds well to the flow routes of the winter Guangdong Coastal Current and to the surface northeastward of the SCS Warm current (Fig. 9) (Liu et al., 2010c).

5.2.2. Sediment transport in deep water

Deep-water sedimentary systems have been receiving intensive attention during recent decades, because of their crucial importance for natural resource (e.g., deep-sea mineral deposits and hydrocarbon reservoirs) and academic research (e.g., paleoceanography and paleoclimatology) (Mulder, 2011). The dynamic processes driven by downslope and along-slope transport play a significant role in the construction and shaping of continental margins (Mulder, 2011; Stow et al., 2008). The northern SCS provides an ideal laboratory to investigate deep-water depositional process and their relationship with deep-sea circulation (Liu et al., 2008). Various proxies have revealed that a deep-water current (DWC) may exist that affects sediment transport and deposition in the northern SCS, and reflection seismic profiles show that strong DWC activity leads to a complex sedimentary process in the northeastern SCS (e.g. Lüdmann et al., 2005; Shao et al., 2007; Zheng and Yan et al., 2012). Nevertheless, there is still no detailed information about the full DWC transport route in the SCS after it flows into the northern part of the sea through the Luzon Strait.

Over the years, the definition of contourites has been broadened and they are now considered to be sediments deposited or significantly affected by the action of bottom current (Rebesco et al., 2014). The transport and deposition of contourites, involving many cycles of erosion and deposition under intermittently strong deep-sea currents, produces fine sediments that show some sorting (McCave, 2008). Using the distribution of sediment components as a function of grain size, as well as size parameters to the infer current strength, has been commonplace investigations of for deep-sea sediments (Tegzes et al., 2015). This led McCave (2008) to propose the use of the 10–63 μm silt fraction, “sortable silt”, as a flow-speed indicator, because the grains were more likely to have been deposited individually in response to fluid stresses (McCave et al., 1995a). Changes in the coarseness of the 10–63 μm terrigenous silt fraction in marine sediments across successive layers of current-sorted deposits are considered good indicators of variations in the strength of the depositing current, with coarser sediments indicating intervals of relatively greater near-bottom flow speeds (McCave and Hall, 2006; McCave et al., 1995b). The “sortable silt” fraction thus reflects the degree to which deep-sea sediments have been reworked by currents and is widely used as a proxy of bottom current strength (McCave et al., 2008; McCave et al., 2013; McCave and Hall, 2006). Sortable silt component results from terrigenous sediments show that bottom current flow speeds in the northern SCS are strongly coupled to deep water currents (Fig. 8).

Based on the sortable silt component distribution of surface sediments in the northern SCS, the sediment transport route of the DWC is outlined in Fig. 8 and 9. The high sortable-silt content (25–35%) is distributed in a NE-SW orientation along-margin channels that cut across the continental slope following isobaths. Specifically, after the intrusion of the southward flowing NPDW through the Bashi Channel, the deep ocean current is deflected to the north by the topographic obstacles, flows along the Kaoping slope of Taiwan, and then turns to the southwest along the continental slope. Finally, the bottom current intensifies when it flows through the Xisha trough. Throughout the whole process, the strengthening of bottom water is influenced by slope turbidites and uplifted morphologies (Chen et al., 2014). This is also observed in the other areas, such as Le Danois area, the Galicia Bank and Gulf of Cadiz, topographic obstacles (e.g. mud volcanoes, salt diapirs, tectonic ridges) are known to alter the current pattern and increase the flow speed (Hanebuth et al., 2015; Somoza et al., 2003;Van Rooij et al., 2010). Recently, high-resolution seismic data revealed a series of sediment waves that have migrated upslope, confirming the existence of westward traveling deep currents in front of the SCS slope (Chen et al., 2014; Gong et al., 2012; Gong et al., 2015; Kuang et al., 2014; Li et al., 2013; Zhu et al., 2010). For example, a collisional type of sediment routing system (i.e. Penghu Canyon-southwest Taiwan collision basin) is located along the oblique collision boundary between two crossing margins parallel to the strike of the adjacent orogeny. The axial canyon is supplied with sediments from both flanking continental slopes: the Kaoping Slope and the South China Sea Slope (Zhong et al., 2015). The tectonically active Kaoping Slope is characterized by frequent episodic events such as earth quakes and floods, which allow intense erosion of canyons/channels and mass movements that, act as the principal sediment supply (Hsiung and Yu, 2013). Therefore, high-energy mass flows and sediment gravity-flows dominate over bottom currents on the continental slope of the studied margin, forming erosional features, mass-flow systems and sediment gravity-flow systems.

At the same time, the dominance of the “sortable silt” fraction over other particle sizes in the northern SCS strongly supports the hypothesis of current-controlled sedimentation in the northern SCS (Fig. 9). Furthermore, the DWC transport route gives significant evidence for sediment drift on the northeastern SCS slope, where the DWC might also lead to the accumulation of Taiwan-sourced sediments with high sedimentation rates (Fig. 9). To sum up, transport routes are based on the dynamic partitioning of surface sediments in the northern SCS, where the saltation and graded suspension percentage index (Province B) confirm the inflow of NPDW from the Luzon Strait (Wang, 1999).

6. Conclusions

In this study, mathematical partitioning of sediment grain sizes has been used to investigate the details of source, transport and hydrodynamic environment in the northern SCS. On the basis of spatial distribution characteristics, the study area can be classified into three hydrodynamic provinces. Province A covers the Taiwan Shoal and Dongsha Islands, and extends from the Pearl River estuary to southeastern Hainan Island, which is exposed to longshore currents and local topography. Province B is widespread on the northern slope of the SCS; the formation of the high value areas here is interpreted as the result of interactions between down- and along-slope processes. Province C reached its greatest concentration in the abyssal areas, particularly in the vicinity of Luzon Island, which settles only under calm conditions. The sortable silt distribution of the terrigenous sediments can be used to examine the deep water current route in the deep ocean. Combining the results of the high sortable silt concentrations (25–35%), sediment transport appeared to take place in NE-SW orientated along-margin channels that cut across the continental slope following isobaths. We therefore suggest that these mathematical partitioning methods may have broad applications in environments with complex hydrological conditions.

7. Acknowledgments

This work has been financially supported by the project of the Chinese National

Science Foundation (contracts 41306047; 41676056).

References

Antobreh, A.A., Krastel, S., 2006. Morphology, seismic characteristics and development of Cap Timiris Canyon, offshore Mauritania: a newly discovered canyon preserved-off a major arid climatic region. Marine and Petroleum Geology 23, 37-59.

Boulay, S., Colin, C., Trentesaux, A., Clain, S., Liu, Z., Lauer-Leredde, C., 2007. Sedimentary responses to the Pleistocene climatic variations recorded in the South China Sea. Quaternary Research 68, 162-172.

Boulay, S., Colin, C., Trentesaux, A., Pluquet, F., Bertaux, J., Blamart, D., Buehring, C., Wang, P., 2003. 19. Mineralogy and Sedimentology of Pleistocene Sediment in the South China Sea (ODP Site 1144). In: Prell, W.L., Wang, P., Blum, P., Rea, D.K., Clemens, S.C. (Eds.), Proceedings of the Ocean Drilling Program, Scientific Results, vol. 184, pp. 1-21.

Cai, G.Q., Miao, L., Chen, H.J., Sun, G.H., Wu, J.Q., Xu, Y.H., 2013. Grain size and geochemistry of surface sediments in northwestern continental shelf of the South China Sea. Environment Earth Science 70, 363-380.

Carranza-Edwards, A., Rosales-Hoz, L., Urrutia-Fucugauchi, J., Sandoval-Fortanel, A., Morales de la Garza, E., Lozano Santa Cruz, R., 2005. Geochemical distribution pattern of sediments in an active continental shelf in Southern Mexico. Continental Shelf Research 25, 521-537.

Caruso, M.J., Gawarkiewicz, G.G., Beardsley, R.C., 2006. Interannual variability of the Kuroshio intrusion in the South China Sea. Journal of Oceanography 62, 559-575.

Chen, C.T.A., Wang, S.L., 1998. Influence of intermediate water in the western Okinawa Trough by the outflow from the South China Sea. Journal of Geophysical Research: Oceans 103, 12683-12688.

Chen, G.Q., Yi, L., Chen, S.L., Huang, H.J., Liu, Y.X., Xu, Y.H., Cao, J.R., 2013a. Partitioning of grain-size components of estuarine sediments and implications for sediment transport in southwestern Laizhou Bay, China. Chin. J. Ocean. Limnol.

31, 895-906.

Chen, H., Xie, X.N., Van Rooij, D., Vandorpe, T., Huang, L., Guo, L.Y., Su, M., 2013b. Depositional characteristics and spatial distribution of deep-water sedimentary systems on the northwestern middle-lower slope of the Northwest Sub-Basin, South China Sea. Marine Geophysical Research 34, 239-257.

Chen, H., Xie, X.N., Van Rooij, D., Vandorpe, T., Su, M., Wang, D.X., 2014. Depositional characteristics and processes of alongslope currents related to a seamount on the northwestern margin of the Northwest Sub-Basin, South China Sea. Marine Geology. 355, 36-53.

Chen, L.R., Xu, W.Q., Shen, S.X., Li, A.C., 1986. Mineral assemblages and their distribution pattern in the sediments from the north continental shelf of the South China Sea and the Beibu Gulf. Mar. Sci. 10, 6-10.

Chiu, J.K., Liu, C.S., 2008. Comparison of sedimentary processes on adjacent passive and active continental margins offshore of SW Taiwan based on echo character studies. Basin Research 20, 503-518.

Christiansen, C., Blaesild, P., Dalsgaard, K., 1984. Re-interpreting ‘segmented’grain-size curves. Geological Magazine 121, 47-51.

Chung, Y., Chang, H.C., Hung, G.W., 2004. Particulate flux and 210Pb determined on the sediment trap and core samples from the northern South China Sea. Continental Shelf Research 24, 673-691.

Clemens, S.C., Prell, W.L., 1990. Late Pleistocene variability of Arabian Sea summer monsoon winds and continental aridity: Eolian records from the lithogenic component of deep-sea sediments. Paleoceanography 5, 109-145.

Cunningham, M.J., Hodgson, S., Masson, D.G., Parson, L.M., 2005. An evaluation of along- and down-slope sediment transport processes between Goban Spur and Brenot Spur on the Celtic margin of the Bay of Biscay. Sedimentary Geology 179, 99-116.

Dong, L.X., Su, J.L., Wong, L.A., Cao, Z.Y., Chen, J.-C., 2004. Seasonal variation and dynamics of the Pearl River plume. Continental Shelf Research 24, 1761-1777.

Yuan, D.L., 2002. A numerical study of the South China Sea deep circulation and its relation to the Luzon Strait transport. Acta Oceanol Sin 21, 187-202.

Du, X.-Q., Gao, S., Li, Y., 2010. Hydrodynamic processes and bedload transport associated with large-scale sandwaves in the Taiwan Strait. Journal of Coastal Research, 688-698.

Ellison, C.R., Chapman, M.R., Hall, I.R., 2006. Surface and deep ocean interactions during the cold climate event 8200 years ago. Science 312, 1929-1932.

Ellwood, B.B., Balsam, W.L., Roberts, H.H., 2006. Gulf of Mexico sediment sources and sediment transport trends from magnetic susceptibility measurements of surface samples. Marine Geology 230, 237-248.

Ellwood, B.B., Ledbetter, M.T., 1977. Antarctic bottom water fluctuations in the Vema Channel: Effects of velocity changes on particle alignment and size. Earth and Planetary Science Letters 35, 189-198.

Fang, G.H., Fang, W.D., Fang, Y., Wang, K., 1998. A survey of studies on the South China Sea upper ocean circulation. Acta Oceanographica Taiwanica 37, 1-16.

Fang, W.D., Guo, P., Liu, C.J., Fang, G.H., Li, S.J., 2015. Observed sub-inertial current variability and volume transport over the continental shelf in the northern South China Sea. Estuarine, Coastal and Shelf Science 157, 19-31.

Fernando, A.G.S., Peleo-Alampay, A.M., Wiesner, M.G., 2007. Calcareous nannofossils in surface sediments of the eastern and western South China Sea. Marine Micropaleontology 66, 1-26.

Folk, R.L., 1966. A review of grain-size parameters. Sedimentology 6, 73-93.

Folk, R.L., Ward, W.C., 1957. Brazos River bar: a study in the significance of grain size parameters. Journal of Sedimentary Research 27, 3-26.

Friedman, G.M., 1979. Differences in size distributions of populations of particles among sands of various origins: addendum to IAS Presidential Address. Sedimentology 26, 859-862.

Gao, S., Collins, M.B., Lanckneus, J., De Moor, G., Van Lancker, V., 1994. Grain size trends associated with net sediment transport patterns: An example from the Belgian continental shelf. Marine Geology 121, 171-185.

Ge, Q., Liu, J.P., Xue, Z., Chu, F.Y., 2014. Dispersal of the Zhujiang River (Pearl River) derived sediment in the Holocene. Acta Oceanol Sin 33, 1-9.

Ghoshal, K., Mazumder, B.S., Purkait, B., 2010. Grain-size distributions of bed load: Inferences from flume experiments using heterogeneous sediment beds. Sedimentary Geology 223, 1-14.

Gong, C.L., Wang, Y.M., Peng, X.C., Li, W.G., Qiu, Y., Xu, S., 2012. Sediment waves on the South China Sea Slope off southwestern Taiwan: implications for the intrusion of the Northern Pacific Deep Water into the South China Sea. Marine and Petroleum Geology 32, 95-109.

Gong, C.L., Wang, Y.M., Xu, S., Pickering, K.T., Peng, X.C., Li, W.G., Yan, Q., 2015. The northeastern South China Sea margin created by the combined action of down-slope and along-slope processes: Processes, products and implications for exploration and paleoceanography. Marine and Petroleum Geology 64, 233-249.

Hanebuth, T.J.J., Zhang, W., Hofmann, A.L., Lowemark, L.A., Scwenk, T., 2015. Oceanic density fronts steering bottom-current induced sedimentation deduced from 50 ka contourite-drift record and numerical modeling (off NW Spain). Quat. Sci. Rev. 112, 207-225

He, Y.L., Xie, X.N., Kneller, B.C., Wang, Z.F., Li, X.S., 2013. Architecture and controlling factors of canyon fills on the shelf margin in the Qiongdongnan Basin, northern South China Sea. Marine and Petroleum Geology 41, 264-276.

Hovan, S., (1995). Late Cenozoic atmospheric circulation intensity and climatic history recorded by Eolian deposition in the Eastern Equatorial Pacific Ocean, Leg 138, Process Ocean Drilling. Program: Scientific Results, 138, 615-625.

Hsiung, K.-H., Yu, H.-S., 2013. Sediment dispersal system in the Taiwan–South China Sea collision zone along a convergent margin: A comparison with the Papua New Guinea collision zone of the western Solomon Sea. Journal of Asian Earth Sciences 62, 295-307.

Hu, B.Q., Li, J., Cui, R.Y., Wei, H.L., Zhao, J.T., Li, G.G., Fang, X.S., Ding, X., Zou, L., Bai, F.L., 2014. Clay mineralogy of the riverine sediments of Hainan Island, South China Sea: Implications for weathering and provenance. Journal of Asian Earth Sciences 96, 84-92.

Hu, J.Y., Kawamura, H., Hong, H., Qi, Y.Q., 2000a. A review on the currents in the South China Sea: seasonal circulation, South China Sea warm current and Kuroshio intrusion. Journal of Oceanography 56, 607-624.

Hu, Z.Z., Latif, M., Roeckner, E., Bengtsson, L., 2000b. Intensified Asian summer monsoon and its variability in a coupled model forced by increasing greenhouse gas concentrations. Geophysical Research Letters 27, 2681-2684.

Huang, J., Li, A.C., Wan, S.M., 2011. Sensitive grain size records of Holocene East Asian summer monsoon in sediments of northern South China Sea slope. Quaternary Research 75, 734-744.

Huang. K.F., You. C.F., Chung. C.H., Lin. Y.H., Liu, Z.F., 2014. Tracing the Nd isotope evolution of North Pacific Intermediate and Deep Waters through the last deglaciation from the South China Sea sediments. Journal Asian Earth Science 79, 564-573.

Jiang, T., Xie, X.N., Wang, Z.F., Li, X.S., Zhang, Y.Z., Sun, H., 2013. Seismic features and origin of sediment waves in the Qiongdongnan Basin, northern South China Sea. Marine Geophysical Research 34, 281-294.

Kissel, C., Laj, C., Kienast, M., Bolliet, T., Holbourn, A., Hill, P., Kuhnt, W., Braconnot, P., 2010. Monsoon variability and deep oceanic circulation in the western equatorial Pacific over the last climatic cycle: Insights from sedimentary magnetic properties and sortable silt. Paleoceanography 25, PA3215.

Kuang, Z.G., Zhong, G.F., Wang, L.L., Guo, Y.Q., 2014. Channel-related sediment waves on the eastern slope offshore Dongsha Islands, northern South China Sea. Journal of Asian Earth Sciences 79, 540-551.

Le Roux, J., Rojas, E., 2007. Sediment transport patterns determined from grain size parameters: Overview and state of the art. Sedimentary Geology 202, 473-488.

Li, C.F., Zhou, Z.Y., Hao, H.J., Chen, H.J., Wang, J.L., Chen, B., Wu, J.S., 2008. Late Mesozoic tectonic structure and evolution along the present-day northeastern

South China Sea continental margin. Journal of Asian Earth Sciences 31, 546-561.

Li, G., Yan, W., Zhong, L.F., Xia, Z., Wang, S., 2015. Provenance of heavy mineral deposits on the northwestern shelf of the South China Sea, evidence from single-mineral chemistry. Marine Geology 363, 112-124.

Li, G., Yan, W., Zhong, L.F., 2016. Element geochemistry of offshore sediments in the northwestern South China Sea and the dispersal of Pearl River sediments. Progress in Oceanography 141, 17-29.

Li, H., Wang, Y.M., Zhu, W.L., Xu, Q., He, Y.B., Tang, W., Zhuo, H.T., Wang, D., Wu, J.P., Li, D., 2013. Seismic characteristics and processes of the Plio-Quaternary unidirectionally migrating channels and contourites in the northern slope of the South China Sea. Marine and Petroleum Geology 43, 370-380.

Li, S.L., Gong, C.L., 2016. Flow dynamics and sedimentation of lateral accretion packages in sinuous deep-water channels: A 3D seismic case study from the northwestern South China Sea margin. Journal of Asian Earth Sciences 124, 233-246.

Li, Z.W., Luan, Z.D., Yan, J., Zhuang, L.H., 2011. Characterization of grain size parameters and the provenance analysis of the surface sediment in the outer shelf of the northern South China Sea. Marine Sciences 12, 015.

Liang, W.D., Tang, T.Y., Yang, Y.J., Ko, M.T., Chuang, W.S., 2003. Upper-ocean currents around Taiwan. Deep Sea Research Part II: Topical Studies in Oceanography 50, 1085-1105.

Liu, J.G., Chen, Z., Chen, M.H., Yan, W., Xiang, R., Tang, X.Z., 2010a. Magnetic susceptibility variations and provenance of surface sediments in the South China Sea. Sedimentary Geology 230, 77-85.

Liu, J.G., Chen, Z., Yan, W., Chen, M.H., Yin, X.B., 2010c. Geochemical characteristics of rare earth elements in the fine-grained fraction of surface sediment from South China Sea. Earth Science Journal China University Geoscience 23, 563-571.

Liu, J.G., Xiang, R., Chen, M., Chen, Z., Yan, W., Liu, F., 2011. Influence of the Kuroshio current intrusion on depositional environment in the Northern South China Sea: Evidence from surface sediment records. Marine Geology 285, 59-68.

Liu, J.G., Xiang, R., Chen, Z., Chen, M.H., Yan, W., Zhang, L.L., Chen, H., 2013. Sources, transport and deposition of surface sediments from the South China Sea. Deep Sea Research Part I: Oceanographic Research Papers 71, 92-102.

Liu, J.G., Yan, W., Chen, Z., Lu, J., 2012. Sediment sources and their contribution along northern coast of the South China Sea: Evidence from clay minerals of surface sediments. Continental Shelf Research 47, 156-164.

Liu, J.P., Liu, C.S., Xu, K.H., Milliman, J.D., Chiu, J.K., Kao, S.J., Lin, S.W., 2008a. Flux and fate of small mountainous rivers derived sediments into the Taiwan Strait. Marine Geology 256, 65-76.

Liu, J.T., Huh, C.A., You, C.F., 2009a. Fate of Terrestrial Substances in the Gaoping (Kaoping) Shelf/Slope and in the Gaoping Submarine Canyon off SW Taiwan. Journal of Marine Systems 76, 367-368.

Liu, S.M., Zhang, W.G., He, Q., Li, D.J., Liu, H., Yu, L.Z., 2010b. Magnetic properties of East China Sea shelf sediments off the Yangtze Estuary: Influence of provenance and particle size. Geomorphology 119, 212-220.

Liu, Y.L., Gao, S., Wang, Y.P., Yang, Y., Long, J.P., Zhang, Y.Z., Wu, X.D., 2014. Distal mud deposits associated with the Pearl River over the northwestern continental shelf of the South China Sea. Marine Geology 347, 43-57.

Liu, Z.F., Colin, C., Huang, W., Le, K.P., Tong, S.Q., Chen, Z., Trentesaux, A., 2007. Climatic and tectonic controls on weathering in south China and Indochina Peninsula: Clay mineralogical and geochemical investigations from the Pearl, Red, and Mekong drainage basins. Geochemistry, Geophysics, Geosystems 8, Q05005.

Liu, Z.F., Colin, C., Li, X.J., Zhao, Y.L., Tuo, S.T., Chen, Z., Siringan, F.P., Liu, J.T., Huang, C.-Y., You, C.-F., 2010c. Clay mineral distribution in surface sediments of the northeastern South China Sea and surrounding fluvial drainage basins: Source and transport. Marine Geology 277, 48-60.

Liu, Z.F., Tuo, S.T., Colin, C., Liu, J.T., Huang, C.-Y., Selvaraj, K., Chen, C.-T.A., Zhao, Y.L., Siringan, F.P., Boulay, S., 2008b. Detrital fine-grained sediment contribution from Taiwan to the northern South China Sea and its relation to regional ocean circulation. Marine Geology 255, 149-155.

Liu, Z., Xia, D., 2004. Tidal sands in the China Seas. Beijing: China Ocean Press.

Liu, Z.F., Zhao, Y.L., Colin, C., Siringan, F.P., Wu, Q., 2009b. Chemical weathering in Luzon, Philippines from clay mineralogy and major-element geochemistry of river sediments. Applied Geochemistry 24, 2195-2205.

Liu, Z.F., Zhao, Y.L., Colin, C., Stattegger, K., Wiesner, M.G., Huh, C.-A., Zhang, Y.W., Li, X.J., Sompongchaiyakul, P., You, C.-F., 2016. Source-to-Sink transport processes of fluvial sediments in the South China Sea. Earth-Science Reviews. 153, 238-273.

Lüdmann, T., Wang, P.X., 2001. Plio–Quaternary sedimentation processes and neotectonics of the northern continental margin of the South China Sea. Marine Geology 172, 331-358.

Lüdmann, T., Wong, H.K., 1999. Neotectonic regime on the passive continental margin of the northern South China Sea. Tectonophysics 311, 113-138.

Luo, C.X., Zheng, Z., Zou, H.X., Pan, A.D., Fang, G., Bai, J.J., Li, J., Yang, M.X., 2013. Palaeoenvironmental significance of grain-size distribution of river flood deposits: a study of the archaeological sites of the Apengjiang River Drainage, upper Yangtze region, Chongqing, China. Journal of Archaeological Science 40, 827-840.

McCave, I., 1978. Grain-size trends and transport along beaches: example from eastern England. Marine Geology 28, M43-M51.

McCave, I., 2008. Size sorting during transport and deposition of fine sediments: sortable silt and flow speed. Contourites. Developments in Sedimentology 60, 121-142.

McCave, I.N., Carter, L., Hall, I.R., 2008. Glacial–interglacial changes in water mass structure and flow in the SW Pacific Ocean. Quaternary Science Reviews 27, 1886-1908.

McCave, I.N., Crowhurst, S.J., Kuhn, G., Hillenbrand, C.D., Meredith, M.P., 2013. Minimal change in Antarctic Circumpolar Current flow speed between the last glacial and Holocene. Nature Geoscience., 7, 113-116.

McCave, I.N., Manighetti, B., Beveridge, N., 1995a. Circulation in the glacial

North Atlantic inferred from grain-size measurements. Nature 374, 149-152.

McCave, I.N., Hall, I.R., 2006. Size sorting in marine muds: Processes, pitfalls, and prospects for paleoflow-speed proxies. Geochem. Geophys. Geosyst. 7, Q10n05.

McCave, I.N., Manighetti, B., Robinso, S.G., 1995b. Sortable silt and fine sediment size/composition slicing: Parameters for palaeocurrent speed and palaeoceanography. Paleoceanography 10, 593-610.

Milliman, J.D., Farnsworth, K.L., 2011. River discharge to the coastal ocean: a global synthesis. Cambridge University Press.

Miousse, L., Bhiry, N., Lavoie, M., 2003. Isolation and water-level fluctuations of Lake Kachishayoot, Northern Québec, Canada. Quaternary Research 60, 149-161.

Mulder, T., 2011. Gravity processes and deposits on continental slope, rise and abyssal plains. Deep-sea sediments, 25-148.

Negre, C., Zahn, R., Thomas, A.L., Masque, P., Henderson, G.M., Martinez-Mendez, G., Hall, I.R., Mas, J.L., 2010. Reversed flow of Atlantic deep water during the Last Glacial Maximum. Nature 468, 84-88.

Nordstrom, K., 1981. Differences in grain size distribution with shoreline position in a spit environment. Northeastern Geology 3, 252-258.

Oldfield, F., Hao, Q., Bloemendal, J., GIBBS-EGGAR, Z., Patil, S., Guo, Z., 2009. Links between bulk sediment particle size and magnetic grain-size: general observations and implications for Chinese loess studies. Sedimentology 56, 2091-2106.

Oldfield, F., Yu, L., 1994. The influence of particle size variations on the magnetic properties of sediments from the north-eastern Irish Sea. Sedimentology 41, 1093-1108.

Pan, J.Y., Gu, Y.Z., 2016. Cruise observation and numerical modeling of turbulent mixing in the Pearl River estuary in summer. Continental Shelf Research 120, 122-138.

Purkait, B., 2006. Grain-size distribution patterns of a point bar system in the

Usri River, India. Earth Surface Processes and Landforms 31, 682-702.

Qu, T.D., Girton, J.B., Whitehead, J.A., 2006. Deepwater overflow through Luzon strait. Journal of Geophysical Research: Oceans (1978–2012) 111.

Qu, T.D., Kim, Y.Y., Yaremchuk, M., Tozuka, T., Ishida, A., Yamagata, T., 2004. Can Luzon Strait Transport Play a Role in convey. Journal of Climate 17, 3644-3657.

Qu, T.D., Song, Y.T., Yamagata, T., 2009. An introduction to the South China Sea throughflow: its dynamics, variability, and application for climate. Dynamics of Atmospheres and Oceans. 47, 3-14.

Rea, D.K., Janecek, T.R., 1981. Mass-accumulation rates of the non-authigenic inorganic crystalline (eolian) component of deep-sea sediments from the western mid-Pacific mountains. Deep Sea Drilling Project Site 463. Initial Reports, DSDP. 62, pp, 653-659.

Rebesco, M., Hernandez-Molina, F.J., van Rooij, D., Wahlin, A., 2014. Contourites and Associated Sediments Controlled by Deep-Water Circulation Processes: State of the Art and Future Considerations. Marine Geology 352, 111-154.

Reeder, D.B., Ma, B.B., Yang, Y.J., 2011. Very large subaqueous sand dunes on the upper continental slope in the South China Sea generated by episodic, shoaling deep-water internal solitary waves. Marine Geology 279, 12-18.

Self, R.P., 1977. Longshore variation in beach sands Nautla area, Veracruz, Mexico. Journal of Sedimentary Research 24, 151-158.

Shao, L., Li, X.J., Geng, J.H., Pang, X., Lei, Y.C., Qiao, P.J., Wang, L.L., Wang, H.B., 2007. Deep water bottom current deposition in the northern South China Sea. Science in China Series D: Earth Sciences 50, 1060-1066.

Shao, L., Qiao, P.J., Pang, X., Wei, G.J., Li, Q.Y., Miao, W.L., Li, A., 2009. Nd isotopic variations and its implications in the recent sediments from the northern South China Sea. Chinese Science Bulletin 54, 311-317.

Shaw, P.-T., Chao, S.-Y., 1994. Surface circulation in the South China Sea. Deep Sea Research Part I: Oceanographic Research Papers 41, 1663-1683.

Shepard, F.P., 1954. Nomenclature based on sand-silt-clay ratios. Journal of Sedimentary Research 24, 151-158.

Shepard, F.P., Emery, K.O., 1973. Congo submarine canyon fan valley. American Association of Petroleum Geologists Bulletin 57, 1679-1691.

Somoza, L., Diaz-del-Rio, V., Leon, P., Ivanov, M., Fernandez-Puga, M.C., Gardner, J.M., Hernández-Molina, F.J., Pinheiro, L.M., Rodero, J., Lobato, A., Maestro, A., Vázquez, J.T., Medialdea, T., Fernández-Salas, L.M., 2003. Seabed morphology and hydrocarbon seepage in the Gulf of Cádiz mud volcano area: Acoustic imagery, multibeam and ultra-high resolution seismic data. Marine Geology 195, 153-176.

Stow, D.A., Faugères, J.-C., Howe, J.A., Pudsey, C.J., Viana, A.R., 2002. Bottom currents, contourites and deep-sea sediment drifts: current state-of-the-art. Geological Society, London, Memoirs 22, 7-20.

Stow, D.A.V., Hunter, S., Wilkinson, D., Hernández-Molina, F.J., 2008. Chapter 9 The Nature of Contourite Deposition, in: Rebesco, M., Camerlenghi, A. (Eds.), Developments in Sedimentology. Elsevier, pp. 143-156.

Stow, D.A.V., Hernandez-Molina, F.J., Llave, E., Sayago-Gil, M., Diaz-del Rio, V., Branson, A., 2009. Bedform-velocity matrix: the estimation of bottom current velocity from bedform observation. Geology 37, 327-330.

Sun, D., Bloemendal, J., Rea, D., Vandenberghe, J., Jiang, F., An, Z., Su, R., 2002. Grain-size distribution function of polymodal sediments in hydraulic and aeolian environments, and numerical partitioning of the sedimentary components. Sedimentary Geology 152, 263-277.

Sval'nov, V., Alekseeva, T., 2006. Characteristics of the grain-size composition of deep-water oceanic sediments. Lithology and Mineral Resources 41, 201-214.

Tegzes, A.D., Jansen, E., Telford, R.J., 2015. Which is the better proxy for paleo-current strength: Sortable-silt mean size (ss) or sortable-silt mean grain diameter (d_{SS})? A case study from the Nordic Seas. Geochemistry, Geophysics, Geosystems 16, 3456-3471.

Tian, J., Yang, Q., Liang, X., Xie, L., Hu, D., Wang, F., Qu, T., 2006. Observation of Luzon Strait transport. Geophysical Research Letters 33.

Van Rooij, D., Iglesias, J., Hernandez-Molina, F.J., Ercilla, G., Gomez-Ballesteros, M., Casas, D., Llave, E., De Hauwere, A., Garcia-Gil, S., Acosta, J., Henriet, J.P., 2010. The Le Danois contourite depositional system: interactions between the Mediterranean outflow water and the upper Cantabrian slope (north Iberian margin). Marine Geology 274, 1-20.

Visher, G.S., 1969. Grain size distributions and depositional processes. Journal of Sedimentary Research 39.

Wan, S., Li, A., Clift, P.D., Stuut, J.-B.W., 2007. Development of the East Asian monsoon: mineralogical and sedimentologic records in the northern South China Sea since 20 Ma. Palaeogeography, Palaeoclimatology, Palaeoecology 254, 561-582.

Wan, S.M., Li, A., Clift, P.D., Wu, S., Xu, K., Li, T., 2010. Increased contribution of terrigenous supply from Taiwan to the northern South China Sea since 3Ma. Marine Geology 278, 115-121.

Wang, G.H., Xie, S.P., Qu, T.D., Huang, R.X., 2011. Deep South China Sea circulation. Geophysical Research Letters 38.

Wang, P.X., 1999. Response of Western Pacific marginal seas to glacial cycles: paleoceanographic and sedimentological features. Marine Geology 156, 5-39.

Wang, P.X., Li, Q.Y., 2009. History of the South China Sea–A Synthesis, The South China Sea. Springer, pp. 487-496.

Wang, X., Dong, Z., Zhang, J., Qu, J., Zhao, A., 2003. Grain size characteristics of dune sands in the central Taklimakan Sand Sea. Sedimentary Geology 161, 1-14.

Wang, Y., Ren, M.-e., Zhu, D., 1986. Sediment supply to the continental shelf by the major rivers of China. Journal of the Geological Society 143, 935-944.

Webster, P.J., 1994. The role of hydrological processes in ocean-atmosphere interactions. Reviews of Geophysics 32, 427-476.

Wei, G.J., Liu, Y., Ma, J.L., Xie, L.H., Chen, J.F., Deng, W.F., Tang, S., 2012. Nd, Sr isotopes and elemental geochemistry of surface sediments from the South China Sea: implications for provenance tracing. Marine Geology 319-322, 21-34.

Wu, C.-R., Chiang, T.-L., 2007. Mesoscale eddies in the northern South China Sea. Deep Sea Research Part II: Topical Studies in Oceanography 54, 1575-1588.

Wyrtki, K., 1961. Physical oceanography of the southeast Asian waters. Naga Rep. 2, 195 pp. Scripps Institution of Oceanography. La Jolla, Calif.

Xiao, J., Chang, Z., Si, B., Qin, X., Itoh, S., Lomtatidze, Z., 2009. Partitioning of the grain-size components of Dali Lake core sediments: evidence for lake-level changes during the Holocene. J Paleolimnol 42, 249-260.

Xiao, J., Fan, J., Zhou, L., Zhai, D., Wen, R., Qin, X., 2013. A model for linking grain-size component to lake level status of a modern clastic lake. Journal of Asian Earth Sciences 69, 149-158.

Xie, L., Tian, J., Hu, D., Wang, F., 2009a. A quasi-synoptic interpretation of water mass distribution and circulation in the western North Pacific II: Circulation. Chin. J. Ocean. Limnol. 27, 955-965.

Xie, L., Tian, J., Hu, D., Wang, F., 2009b. A quasi-synoptic interpretation of water mass distribution and circulation in the western North Pacific: I. Water mass distribution. Chin. J. Ocean. Limnol. 27, 630-639.

Xu, K., Milliman, J.D., Li, A., Liu, J.P., Kao, S.-J., Wan, S., 2009. Yangtze-and Taiwan-derived sediments on the inner shelf of East China Sea. Continental Shelf Research 29, 2240-2256.

Xue, H., Chai, F., Pettigrew, N., Xu, D., Shi, M., Xu, J., 2004. Kuroshio intrusion and the circulation in the South China Sea. Journal of Geophysical Research: Oceans 109, C02017.

Yan, P., Deng, H., Liu, H., Zhang, Z., Jiang, Y., 2006. The temporal and spatial distribution of volcanism in the South China Sea region. Journal of Asian Earth Sciences 27, 647-659.

Yi, L., Yu, H., Ortiz, J.D., Xu, X., Qiang, X., Huang, H., Shi, X., Deng, C., 2012. A reconstruction of late Pleistocene relative sea level in the south Bohai Sea, China, based on sediment grain-size analysis. Sedimentary Geology 281, 88-100.

Yu, H.-S., Song, G.-S., 2000. Submarine Physiographic Features in Taiwan Region and Their Geological Singificance. Journal Geological Society of China-Taiwan 43, 267-286.

Yuan, D., Han, W., Hu, D., 2006. Surface Kuroshio path in the Luzon Strait area derived from satellite remote sensing data. Journal of Geophysical Research: Oceans 111.

Zhang, J., Wang, D.R., Jennerjahn, T., Dsikowitzky, L., 2013. Land–sea interactions at the east coast of Hainan Island, South China Sea: A synthesis. Continental Shelf Research 57, 132-142.

Zhang, W., Yu, L., 2003. Magnetic properties of tidal flat sediments of the Yangtze Estuary and its relationship with particle size. Science in China Series D: Earth Sciences 46, 954-966.

Zhang, Q.H., Fan, H.M., Qu, Y.Y., 2006. Kuroshio intrusion into the South China Sea. Journal Hydrodynamic. 18, 702-713.

Zhao, W., Zhou, C., Tian, J., Yang, Q., Wang, B., Xie, L., Qu, T., 2014. Deep water circulation in the Luzon Strait. Journal of Geophysical Research: Oceans 119, 790-804.

Zheng, H.-B., Yan, P., 2012. Deep-water bottom current research in the northern South China Sea. Marine Georesources & Geotechnology 30, 122-129.

Zhong, L.F., Li, G., Yan, W., Xia, B., Feng, Y.X., Miao, L., Zhao, J.X., Using zircon U-Pb ages to constrain the provenance and transport of heavy minerals within the northwestern shelf of the South China Sea. Journal of Asian Earth Sciences 134, 176-190.

Zhong, G.F., Cartigny, M.J., Kuang, Z.G., W, L.L., 2015. Cyclic steps along the South Taiwan shoal and West Penghu submarine canyons on the northeastern continental slope of the South China Sea. Geological Society of America Bulletin 127, 804-824.

Zhu, M., Graham, S., Pang, X., McHargue, T., 2010. Characteristics of migrating submarine canyons from the middle Miocene to present: implications for paleoceanographic circulation, northern South China Sea. Marine and Petroleum Geology 27, 307-319.

Figure Captions:

Fig. 1. (a) Sketch map of the South China Sea and surrounding basins (modified from Hu et al., (2014)); the red solid arrows are the intrusion of the North Pacific Deep Water into SCS into the Luzon Strait (Lüdmann et al., 2005; Gong et al., 2012). (b) Monsoon winds and current system of northern South China Sea. Monsoon winds after (Webster, 1994); surface current after (Fang et al., 1998) ; deep current deduced from (Qu et al., 2006); longshore current after (Wang et al., 1986). Numbers for winter and summer surface currents (Fang et al., 1998): 1, Loop Current; 2, SCS Branch of Kuroshio; 3, NW Luzon Cyclonic Eddy; 4, NW Luzon Coastal Current; 5, SCS Warm Current; 6, Guangdong Coastal Current. Large arrows with numbers indicate annual sediment loading of surrounding major sources (from Zhang et al., 2013; Milliman and Farnsworth, 2011). (For interpretation of the references to colour in this figure legend, the reader is referred to the web version of this article.)

Fig. 2. Locations of surface sediment samples in the northern South China Sea (see Supplement Table A1 for their detailed GPS locations).

Fig. 3. Spatial distribution of (a) contents of gravel (b) sand (c) silt (d) clay in sea-bottom terrigenous sediments.

Fig. 4. (a) Spatial distribution of contents of median grain size of surface sediments; (b) Variances of median grain size of surface sediments with water depth in the northern South China Sea.

Fig. 5. Spatial distribution of contents of (a1) traction, (b1) saltation, (c1) graded suspension, (d1) uniform suspension; the corresponding typical frequency curves and cumulative probability curves (a2, b2, c2 and d2) of grain size distribution of terrigenous sediment from northern South China Sea.

Fig. 6. Hydrodynamic provinces in the northern SCS according to grain size components. A, B and C denote high traction, transition and uniform suspension province, respectively; Among them, A1 area is on the Taiwan Shoal and Dongsha Islands; A2 area is extending from the Pearl River estuary to the southeast Hainan Island. Province B consists of high saltation and graded suspension. Province C consists of uniform suspension.

Fig. 7. Magnetic susceptibility (MS) distribution from the northern South China Sea. MS trends representing high detrital sediment flow trajectories into the northern South China Sea (modified from Liu et al. (2010) and Li et al. (2014)).

Fig. 8. Sortable Silt (SS, 10-63μm) distribution from the northern of South China Sea. The red shadowed areas represent the sediment wave zones (Jiang et al., 2013).

Fig. 9. Schematic map showing the main sediment sources and transport patterns in the northern SCS. Black symbols fork (×) represent sedimentary drifts on SCS northern slope, based on explanation of seismic profiles (Shao et al., 2007); The brown arrows are the inferred deep current circulation pathways in the northern SCS (Chen et al., 2014; Li et al., 2013; Zheng and Pin, 2012); The red shadow areas represent the sediment waves fields (Gong et al., 2012; Jiang et al., 2013). The red dotted lines represent the main canyon route in the northern SCS. PHC=Penghu Canyon; KPC=Kaoping Canyon; FC=Formosa Canyon.

Table 1. Locations and particle size information of surface sediment samples in the northern South China Sea.

Num	Sample no.	Long (N)	Lat (E)	Depth (m)	Granule content (%)				Grain size parameters				
					Gravel	Sand	Silt	Clay	Mz	Md	Skf	Kg	σi
1	09E401	117.30	21.70	292		0.35	76.94	22.71	6.89	6.75	-0.19	1.05	1.50
2	08E703	115.01	20.02	675		0.07	77.62	22.31	6.86	6.65	-0.26	1.07	1.54
3	10JJW-70	111.50	19.00	153		4.48	77.22	18.30	6.39	6.22	-0.21	1.06	1.74
4	09E420	113.53	18.02	1929		0.41	58.63	40.97	7.77	7.67	-0.14	1.07	1.34

5	09KJ16	111.99	17.99	2310	0.29	65.95	33.76	7.44	7.34	-0.14	1.05	1.51
6	09E601	109.79	18.19	70	8.35	53.31	38.34	7.26	7.26	0.01	0.88	2.35
7	11E406	119.74	18.74	3415	16.52	54.38	29.10	6.54	6.55	-0.04	0.78	2.38
8	11E205	117.45	21.39	652	66.33	24.73	8.94	3.35	2.51	-0.58	1.05	2.49
9	10E706	113.80	21.26	65	4.78	63.65	31.57	7.03	6.89	-0.11	0.91	2.10
10	10E416	110.01	18.01	98	64.87	17.63	17.50	4.55	3.17	-0.70	0.80	2.75
11	10E702	114.75	20.24	180	22.37	51.65	25.99	6.10	6.11	0.03	0.99	2.84
12	09E107	115.90	21.10	299	26.07	57.54	16.39	5.60	5.50	-0.12	1.01	2.36
13	09E106	115.71	21.30	122	66.10	26.27	7.63	4.08	3.46	-0.57	1.45	1.89
14	10E704	114.25	20.75	85	38.35	38.13	23.53	5.26	5.51	0.03	0.66	3.24
15	09E424	111.45	17.98	1947	0.06	63.35	36.59	7.53	7.33	-0.19	0.94	1.73
16	10KJ19	110.50	17.99	157	0.83	61.71	37.46	7.54	7.28	-0.17	0.89	1.94
17	10E703	114.50	20.50	117	39.06	44.70	16.24	4.99	4.58	-0.27	0.93	2.69
18	08E525	114.60	19.40	1190		56.62	43.39	7.89	7.70	-0.18	0.94	1.58
19	09E402	119.95	21.00	3370	7.48	60.71	31.81	6.90	6.84	-0.07	0.85	2.22
20	11E109	117.97	19.01	3739	0.07	49.40	50.53	8.10	7.99	-0.07	0.94	1.69
21	10E413	113.06	18.03	158		48.61	51.39	8.20	8.02	-0.17	0.94	1.48
22	10JJW-10	118.99	20.51	2105	0.00	50.18	49.82	8.14	7.96	-0.17	0.97	1.46
23	08E524	112.56	19.66	150	25.55	56.72	17.73	5.66	5.35	-0.24	0.97	2.33
24	11E208	114.50	22.49	35	92.19	4.82	2.99	2.29	2.27	-0.36	2.71	1.04
25	10JJW-07	118.95	21.48	2801		46.73	53.27	8.27	8.08	-0.16	0.93	1.48
26	11E403	120.00	20.38	3536	0.14	59.08	40.78	7.78	7.59	-0.18	0.97	1.60
27	10JJW-76	111.76	20.25	79	37.91	37.97	24.12	5.74	5.46	-0.19	0.73	2.76
28	10E306	118.97	22.04	1396	1.64	64.02	34.35	7.35	7.15	-0.15	0.96	1.88
29	08E702	115.52	19.50	2365	0.01	49.35	50.64	8.15	7.99	-0.16	0.98	1.42
30	10JJW-81	113.50	18.54	1468		51.44	48.57	8.10	7.91	-0.17	0.94	1.51
31	09E108	116.40	21.30	318	83.54	10.44	6.02	2.36	1.75	-0.68	3.20	1.90
32	11E109B	116.98	18.97	3763		45.52	54.48	8.29	8.12	-0.17	0.94	1.42
33	11E201	119.33	19.69	2918	0.08	48.81	51.11	8.16	8.01	-0.14	0.98	1.49
34	09E109	116.91	21.51	336	56.36	35.10	8.54	4.08	3.85	-0.47	2.12	1.57
35	10JJW-84	114.74	19.03	2070	0.02	47.48	52.50	8.25	8.05	-0.18	0.95	1.44
36	08E605	117.54	19.99	2346	0.09	56.15	43.75	7.87	7.72	-0.14	0.99	1.59
37	09KJ21	113.02	17.52	1466		47.93	52.07	8.22	8.04	-0.16	0.94	1.49
38	08E517	111.79	19.16	152	28.92	51.38	19.70	5.63	5.15	-0.31	0.91	2.48
39	07E407A	120.00	18.50	1856	1.32	48.37	50.31	7.97	7.98	0.03	0.86	2.02
40	05S2	115.98	19.22	2612	65.81	15.66	18.53	2.85	0.43	-0.85	0.60	3.70
41	08E515	111.80	18.80	205	23.02	52.46	24.52	6.10	5.87	-0.15	0.85	2.54
42	08E522	111.44	19.64	95	47.08	30.72	22.20	5.04	4.62	-0.22	0.69	3.15
43	04E501	112.27	18.35	1564		55.10	44.90	7.95	7.76	-0.17	0.95	1.58
44	06E307	119.47	21.75	2709	0.02	55.06	44.92	7.95	7.76	-0.17	0.95	1.57
45	08E503	111.05	18.72	139	5.06	63.12	31.83	7.07	6.90	-0.12	0.93	2.11
46	06E408	118.03	18.01	3888		57.87	42.13	7.83	7.66	-0.17	0.98	1.54
47	08E516	112.11	19.03	201	40.06	47.41	12.53	4.87	4.67	-0.20	0.99	2.46
48	06Wan	113.70	21.93	64	19.61	44.93	35.46	6.71	7.01	0.12	0.87	2.78

49	06E203	118.36	20.61	2540	0.01	52.47	47.52	8.05	7.87	-0.15	0.96	1.56
50	06E410	116.00	17.98	3865	0.00	52.95	47.05	7.99	7.84	-0.12	0.93	1.65
51	06E103	115.43	21.51	114	13.96	66.88	19.17	5.96	5.39	-0.43	0.98	2.12
52	08E505	111.44	18.57	200	8.82	65.20	25.98	6.57	6.25	-0.23	0.91	2.17
53	04E102	115.07	21.89	71.3	7.44	63.29	29.27	6.78	6.69	-0.10	0.85	2.18
54	08CF4	119.28	22.11	1345	1.70	61.50	36.81	7.50	7.35	-0.11	1.02	1.83
55	08E104	115.31	21.72	104	6.07	69.71	24.22	6.49	6.12	-0.30	0.90	2.06
56	05E204	117.95	20.99	1370	0.02	63.85	36.13	7.63	7.33	-0.26	0.95	1.66
57	08E501	110.67	18.86	95	32.08	35.25	32.67	6.35	6.50	0.03	0.67	2.94
58	08E512	111.03	19.18	91	42.53	32.46	25.01	5.50	5.12	-0.22	0.69	2.97
59	05E707	114.00	21.07	74	51.48	28.98	19.54	4.48	3.22	-0.58	0.70	3.01
60	07A3	114.39	21.84	52	10.02	61.56	28.42	6.65	6.45	-0.16	0.84	2.25
61	04E505	111.51	19.49	110	40.99	38.35	20.66	5.33	4.90	-0.26	0.77	2.77
62	05E304	118.50	22.50	63	90.42	5.45	4.13	2.52	2.49	-0.41	3.49	1.14
63	06E208	116.50	22.50	44	86.46	7.70	5.84	2.48	2.38	-0.48	3.04	1.40
64	06E303	118.25	22.75	30	96.79	1.43	1.77	1.25	1.24	-0.07	1.01	0.49
65	05E202	118.75	20.17	2893	0.01	49.23	50.76	8.18	7.99	-0.17	0.97	1.46
66	07CF15	115.49	19.99	1300	0.04	58.14	41.82	7.79	7.62	-0.15	0.95	1.65
67	08CF-7	115.21	19.92	1155	0.09	61.34	38.58	7.62	7.42	-0.17	0.93	1.74
68	08E518	111.49	19.28	124	38.07	42.87	19.07	5.41	4.80	-0.37	0.85	2.54
69	07CF11	114.57	19.72	1050	0.00	62.00	38.00	7.65	7.42	-0.21	0.94	1.66
70	08E506	111.62	18.70	201	15.02	60.27	24.71	6.37	6.21	-0.13	0.94	2.31
71	07CF6	119.50	22.01	2455	1.25	58.77	39.98	7.66	7.47	-0.12	0.94	1.87
72	04San	109.48	18.22	14	35.83	43.74	20.43	5.60	5.53	-0.11	0.80	2.71
73	07Dan	114.29	22.06	33	3.23	58.41	38.36	7.49	7.33	-0.09	0.93	2.05
74	08E521	111.27	19.65	87	58.99	21.84	19.17	4.02	2.52	-0.63	0.68	3.27
75	08E513	111.29	19.05	129	87.13	5.40	7.47	-0.23	-0.30	-0.57	8.02	1.71
76	08CF-9	116.38	20.19	1001	95.12	2.57	2.32	-0.34	-0.36	-0.20	1.19	0.35
77	04E604	112.75	20.25	95	48.31	39.08	12.61	4.68	4.21	-0.32	0.79	2.48
78	08E201	116.30	22.68	30	88.10	9.06	2.84	2.72	2.66	-0.39	2.52	1.17
79	08E504	111.24	18.64	168	5.99	77.88	16.14	6.12	5.85	-0.30	1.08	1.76
80	07CF3	118.72	22.08	753	0.68	65.64	33.69	7.32	7.13	-0.17	0.95	1.82
81	08CF-15	116.79	20.18	874	19.16	55.35	25.49	6.33	6.96	0.33	1.14	2.52
82	04E602	112.25	20.75	65	37.88	45.10	17.02	5.41	5.29	-0.14	0.78	2.45
83	08E509	110.94	18.99	106	37.44	44.22	18.33	5.46	5.26	-0.17	0.77	2.47
84	08E523	111.97	19.76	107	57.50	33.36	9.13	4.34	3.57	-0.55	0.90	2.14
85	08E519	111.19	19.41	90	71.24	20.05	8.71	3.59	2.49	-0.65	1.03	2.45
86	05E609	114.13	18.77	1575	7.71	57.11	35.18	7.45	7.40	0.15	1.81	2.11
87	S-490	112.00	20.83	53	48.48	37.72	13.79	4.82	4.11	-0.44	0.82	2.40
88	S-50	114.67	22.33	28	20.80	50.65	28.55	6.24	6.82	0.25	1.02	2.76
89	S-697	110.92	20.75	28.5	10.39	69.63	19.98	6.10	5.67	-0.34	0.90	2.00
90	S-493	112.00	20.33	78	40.50	45.97	13.53	5.07	4.71	-0.27	0.83	2.32
91	S-563	111.60	20.72	52	25.15	55.98	18.87	5.86	5.92	-0.03	0.83	2.27
92	S-338	113.00	20.50	86	52.01	37.74	10.25	4.30	3.60	-0.44	0.76	2.41

93	S-303	113.33	20.33	91	31.34	49.51	19.16	5.40	6.10	0.25	0.77	2.89
94	S-68	114.67	21.50	79	22.03	53.02	24.95	6.14	6.58	0.18	0.92	2.57
95	D20-01	110.28	18.59	33	28.37	56.44	15.19	5.49	5.17	-0.27	0.91	2.16
96	D21-03	110.24	18.16	99	66.73	23.64	9.63	4.18	3.21	-0.63	0.93	2.23
97	S-527	111.73	21.50	18.5	2.14	61.56	36.30	7.55	7.41	-0.12	1.07	1.62
98	D15-5	111.09	20.42	41	9.40	65.68	24.92	6.56	6.55	-0.06	0.93	2.05
99	S-513	111.85	21.00	44	17.22	61.17	21.61	6.20	6.31	0.05	1.06	2.29
100	S-62	114.67	22.00	48	22.27	52.00	25.73	6.14	6.57	0.16	0.90	2.59
101	D16-2	111.18	20.01	52	15.59	62.23	22.19	6.29	6.39	0.03	0.96	2.19
102	S-181	114.00	21.27	73	19.01	63.22	17.78	5.85	6.13	0.16	1.18	2.46
103	S-565	111.50	20.33	68	32.54	52.49	14.97	5.41	5.10	-0.26	0.87	2.20
104	S-515	111.83	20.72	58	23.13	56.24	20.64	5.88	5.94	-0.01	0.91	2.43
105	S-123	114.33	21.50	66	11.32	67.63	21.06	6.40	6.44	0.11	1.29	2.27
106	D19-07	111.76	18.28	1702	0.24	69.47	30.29	7.29	7.18	-0.14	1.05	1.49
107	S-298	113.33	21.17	54	75.31	17.38	7.32	3.35	2.18	-0.69	1.90	2.40
108	S-481	112.07	21.25	34.5	35.91	48.55	15.54	5.19	4.87	-0.23	0.87	2.45
109	D15-1	110.70	20.98	17	52.08	40.14	7.78	4.28	3.88	-0.29	0.98	2.21
110	S-66	114.67	21.67	73	87.61	8.71	3.68	3.23	3.18	-0.41	2.92	1.01
111	S-126	114.37	21.15	77	13.53	57.27	29.20	6.70	6.89	0.20	1.26	2.49
112	S-512	111.77	21.17	36	39.04	44.93	16.03	5.30	5.01	-0.22	0.79	2.39
113	S-337	113.00	20.67	78	53.95	33.97	12.08	4.32	3.42	-0.51	0.74	2.53
114	S-119	114.33	21.83	45	6.64	72.77	20.59	6.45	6.32	-0.15	1.01	1.86
115	D21a-03	110.49	17.80	191	10.44	75.90	13.66	5.86	5.61	-0.28	1.12	1.77
116	S-323	113.17	20.00	125	67.16	26.59	6.26	3.65	2.72	-0.62	0.87	2.17
117	S-478	112.08	21.50	21.5	28.09	57.05	14.86	5.45	4.98	-0.37	0.90	2.10
118	D15-4	110.95	20.59	36	8.10	68.79	23.11	6.57	6.64	0.02	0.96	1.86
119	D23a-01	109.47	17.68	97	35.27	51.07	13.67	5.38	5.30	-0.12	0.80	2.19
120	S-474	112.35	20.05	93	50.25	37.25	12.50	4.62	3.97	-0.40	0.79	2.45
121	S-411	112.67	21.00	52	47.79	39.56	12.65	4.80	4.24	-0.36	0.78	2.36
122	S-299	113.33	21.00	60	30.81	49.02	20.18	5.27	5.96	0.22	0.79	3.04
123	S-171	114.00	22.08	26	8.24	65.81	25.95	6.75	6.74	-0.01	1.07	2.00
124	D21-01	109.99	18.32	57	21.92	55.15	22.93	6.07	6.30	0.09	0.94	2.51
125	S-302	113.33	20.50	549	45.60	41.33	13.07	4.78	4.68	-0.12	0.75	2.61
126	S-442	112.33	21.68	7	6.92	63.57	29.51	7.07	7.11	0.07	1.24	1.87
127	S-185	114.00	20.68	87	56.07	35.25	8.69	3.84	2.93	-0.53	0.77	2.49
128	S-186	114.00	20.50	95	86.51	10.67	2.82	2.47	2.39	-0.41	2.56	1.21
129	S-369	113.00	21.67	24	6.20	66.38	27.42	6.98	6.94	0.00	1.19	1.86
130	D20-05	110.85	18.33	156	4.72	76.13	19.14	6.44	6.27	-0.19	1.05	1.76
131	D21-07	111.00	17.70	1740	5.45	73.36	21.20	6.67	6.61	-0.07	1.11	1.72
132	S-127	114.37	20.97	80	38.37	46.71	14.92	4.96	5.24	0.05	0.72	2.80
133	S-290	113.33	21.82	19	5.73	66.42	27.85	6.78	6.66	-0.12	0.91	2.01
134	S-448	112.35	21.18	40	29.08	52.53	18.40	5.54	5.82	0.11	0.85	2.62
135	S-408	112.67	21.33	39	10.19	65.34	24.48	6.58	6.55	-0.01	1.08	2.11
136	S-372	113.00	21.35	39	57.20	31.53	11.28	4.06	3.13	-0.51	0.77	2.60

137	S-449	112.33	21.00	49	38.45	47.30	14.25	5.19	5.38	0.05	0.75	2.54
138	83-6	114.07	19.50	584	4.15	74.85	21.01	6.72	6.60	-0.13	1.12	1.64
139	83-36	109.00	18.23	29	12.41	71.85	15.74	6.07	5.97	0.01	1.35	2.12
140	79-44	115.02	20.50	180	58.09	36.60	5.31	3.67	3.54	-0.15	0.79	2.41
141	79-12	117.00	22.53	44	94.36	5.12	0.52	2.13	2.11	-0.25	1.73	0.92
142	79-38	119.80	21.53	3100	0.47	76.80	22.73	6.84	6.68	-0.20	1.02	1.55
143	82-36	117.67	23.06	40	94.75	4.79	0.47	1.96	1.94	-0.27	1.82	0.82
144	82-7	116.00	22.50	39	50.28	36.98	12.74	4.68	3.97	-0.45	0.83	2.37
145	79-59	115.98	19.52	1930	1.53	67.00	31.47	7.42	7.39	-0.06	1.14	1.27
146	79-16	118.98	22.50	94	69.20	25.08	5.72	3.83	3.21	-0.50	1.24	1.96
147	82-20	117.37	19.46	3250	0.28	61.84	37.87	7.64	7.57	-0.10	1.08	1.33
148	82-2	115.02	17.99	3714	8.68	72.82	18.50	6.19	5.90	-0.22	0.99	1.86
149	82-15	116.99	23.27	24	37.94	47.43	14.63	5.16	5.27	-0.01	0.74	2.52
150	82-23	118.00	21.52	1656	8.21	65.89	25.90	6.93	6.89	0.05	1.39	1.97
151	79-19	116.02	21.98	85	36.21	53.42	10.37	5.00	4.44	-0.49	1.02	1.88
152	79-66	115.98	19.03	3080	5.38	60.84	33.79	7.45	7.42	0.11	1.60	1.71
153	11E407	119.53	18.04	3023	6.41	71.41	22.18	6.78	6.72	0.07	1.51	1.95
154	79-67	116.50	18.97	2760	0.25	69.85	29.91	7.37	7.29	-0.14	1.11	1.30
155	79-64	115.08	19.03	2070	13.93	52.87	33.20	7.18	7.33	0.27	1.83	2.27
156	11E414A	114.51	18.03	3563	12.73	53.49	33.78	6.95	7.25	0.27	1.44	2.47
157	79-27	115.00	21.52	86	12.55	71.39	16.06	6.10	6.03	0.04	1.34	2.16
158	79-24	118.52	22.10	1860	1.30	74.79	23.91	6.95	6.86	-0.12	1.08	1.54
159	79-65	115.48	18.98	2660	1.67	62.01	36.32	7.57	7.52	-0.06	1.13	1.37
160	79-34	118.50	21.47	2360	0.34	67.73	31.92	7.39	7.31	-0.12	1.07	1.41
161	82-14	116.45	19.52	2167	3.74	65.96	30.30	7.31	7.31	0.03	1.28	1.47
162	11E416	112.50	18.03	2439	0.75	68.04	31.22	7.27	7.23	-0.07	1.05	1.53
163	79-54	116.50	19.83	1210	3.21	68.51	28.28	7.01	7.04	-0.01	1.04	1.71
164	79-63	117.97	19.48	3550	3.84	59.88	36.28	7.54	7.52	0.02	1.28	1.48
165	83-10	112.99	19.02	450	17.38	65.64	16.98	5.99	6.02	0.00	1.01	2.11
166	79-55	116.97	19.83	2180	0.41	66.63	32.96	7.41	7.34	-0.09	1.06	1.43
167	79-5	117.50	23.00	44	72.59	20.83	6.58	3.12	2.04	-0.64	1.02	2.44
168	79-30	116.53	21.50	290	32.74	59.14	8.12	4.97	4.76	-0.14	1.18	1.99
169	79-53	116.03	19.85	1500	4.15	73.98	21.87	7.04	6.97	-0.08	1.19	1.32
170	79-1	117.52	23.52	30	40.61	44.50	14.89	4.88	5.11	0.04	0.70	2.81
171	79-18	115.50	22.20	38	19.04	68.54	12.42	5.61	5.38	-0.25	0.95	1.85
172	D20-03	110.53	18.49	104	33.68	49.85	16.48	5.43	5.62	0.06	0.82	2.54
173	S-782	112.62	19.48	170	60.25	31.99	7.76	4.03	3.31	-0.44	0.92	2.30
174	S-803	112.05	20.08	90	53.89	38.33	7.78	4.07	3.70	-0.27	0.93	2.35
175	S-73	114.67	20.67	115	38.78	41.57	19.65	5.45	5.47	-0.04	0.72	2.63
176	S-722	110.87	20.08	30	54.12	31.66	14.22	4.40	3.71	-0.36	0.80	2.80
177	S-747	110.65	20.67	10	87.39	10.84	1.77	3.20	3.18	-0.28	1.76	0.90
178	S-778	112.60	20.13	91	62.08	30.48	7.45	3.82	3.01	-0.50	0.86	2.34
179	S-786	112.42	20.38	77	32.63	55.02	12.36	5.14	5.57	0.17	0.79	2.54
180	S-831	111.50	20.08	72	23.66	59.89	16.45	5.66	5.77	0.08	1.06	2.45

181	S-814	112.00	19.33	160		85.22	11.73	3.05	2.24	2.13	-0.46	2.71	1.29
182	S-789	112.33	19.78	110		67.30	25.29	7.42	3.80	2.87	-0.60	0.88	2.24
183	S-77	114.67	20.00	220		23.68	52.54	23.78	6.11	6.30	0.15	0.94	2.59
184	D18-1	110.73	19.18	50		67.44	22.65	9.92	4.24	3.31	-0.64	1.06	2.18
185	S-71	114.67	21.00	90		36.87	42.93	20.20	5.53	5.68	0.00	0.73	2.68
186	S-791	112.32	19.48	140		37.07	54.40	8.53	4.95	4.79	-0.18	0.89	1.97
187	D21-05	110.57	18.00	169		5.00	77.30	17.70	6.38	6.26	-0.16	1.04	1.70
188	10JJW-75	111.00	19.50	42	6.79	71.58	15.54	6.09	2.56	1.71	-0.44	2.02	2.64
189	10E707B	116.55	21.95	95	12.20	60.81	17.52	9.47	2.52	1.08	-0.54	1.01	3.42
190	06E301	117.79	23.21	37	23.15	64.48	8.54	3.83	0.31	-0.14	-0.52	1.36	2.24
191	04E709	113.50	21.49	42	38.23	50.03	8.81	2.93	-0.28	-0.42	-0.35	1.73	2.24
192	07E201	117.00	23.00	36	28.82	65.78	4.26	1.14	0.44	0.80	0.12	0.92	1.95
193	07E709	113.49	22.49	400	14.35	67.77	12.11	5.78	1.46	0.47	-0.55	2.03	2.91
194	04E606	113.29	19.69	202		82.98	13.73	3.29	2.44	1.96	-0.42	2.27	1.94
195	D22a-02	109.62	17.90	83		68.03	21.14	10.83	4.17	3.10	-0.62	0.90	2.40
196	S-433	112.67	20.40	82	27.82	54.01	13.44	4.73	1.38	0.94	-0.30	1.10	3.09
197	S-301	113.20	20.67	80	10.32	48.39	31.35	9.95	3.84	2.94	-0.28	1.06	3.12
198	79-7	118.47	22.98	26	25.26	67.45	5.87	1.43	0.34	0.82	0.15	1.27	2.00
199	79-22	117.52	21.98	105	6.12	86.46	5.29	2.13	2.42	2.43	0.01	3.25	1.48
200	79-6	117.97	22.94	36	9.54	86.46	3.26	0.75	1.44	1.47	0.32	2.71	1.12
201	82-21	117.84	23.72	30	33.10	47.88	14.88	4.15	1.50	1.48	-0.09	1.03	3.31
202	79-13	117.66	22.52	35	4.73	82.29	10.15	2.83	1.67	1.14	-0.49	3.14	1.98
203	79-3	118.47	23.48	40	35.41	29.42	28.51	6.67	2.33	2.41	-0.01	0.66	3.87
204	83-37	109.17	17.99	71	18.18	70.77	8.40	2.65	1.25	1.84	0.12	1.40	2.41
205	82-12	116.77	22.95	34	25.64	57.21	11.80	5.35	1.18	0.67	-0.38	1.18	2.93

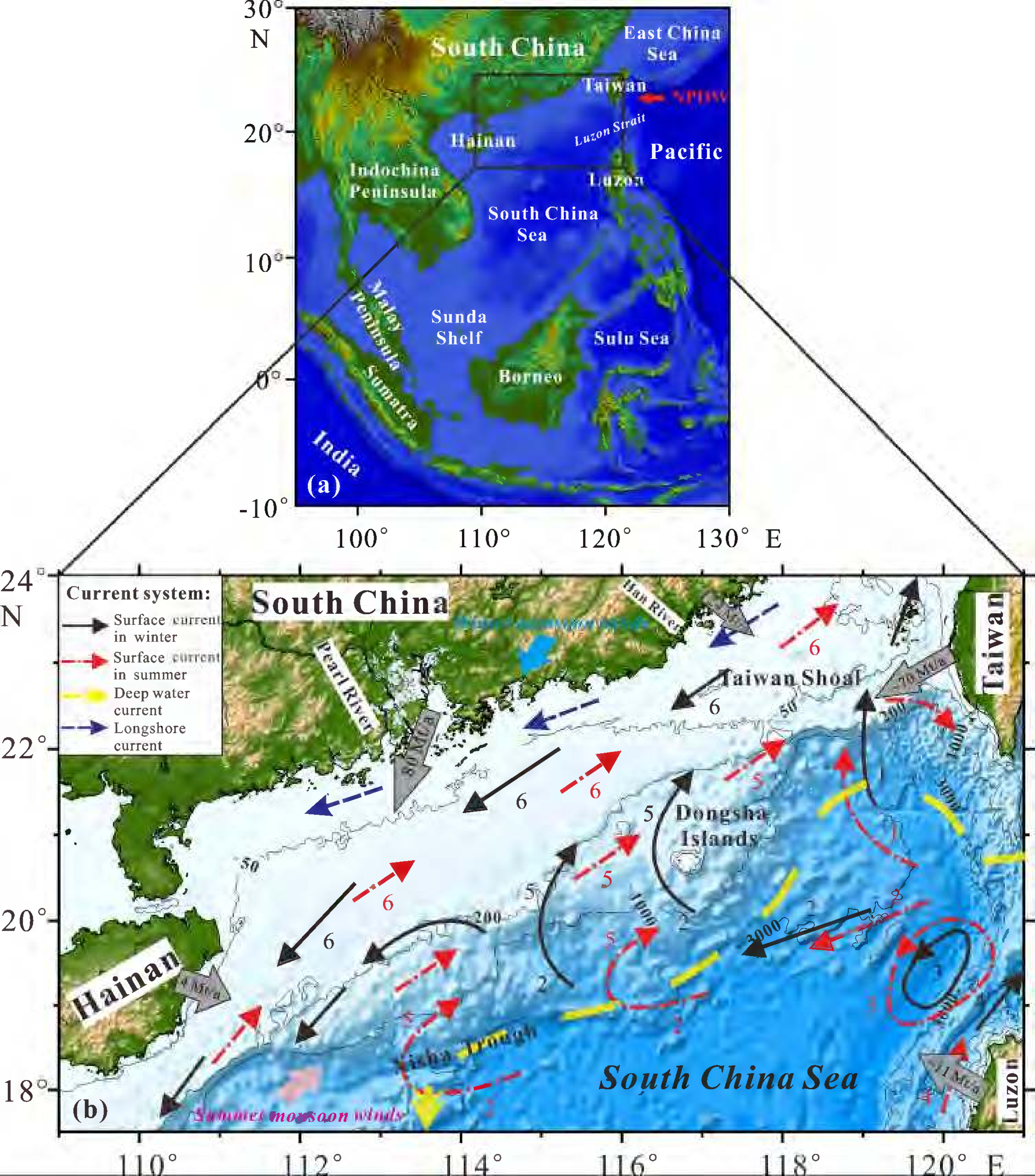
(a)
South China
East China Sea
Taiwan
NPTW
Hainan
Luzon Strait
Pacific
Indochina Peninsula
Luzon
South China Sea
Malay Peninsula
Sunda Shelf
Sulu Sea
Borneo
Sumatra
India
30° N
20°
10°
0°
-10°
100°
110°
120°
130° E
(b)
Current system:
Surface current in winter
Surface current in summer
Deep water current
Longshore current
South China
Winter monsoon winds
Han River
Pearl River
80 Mt/a
70 Mt/a
4 Mt/a
11 Mt/a
Taiwan Shoal
Taiwan
Dongsha Islands
Hainan
Xisha Trough
South China Sea
Summer monsoon winds
Luzon
50
200
1000
2000
3000
6
5
2
24° N
22°
20°
18°
110°
112°
114°
116°
118°
120° E

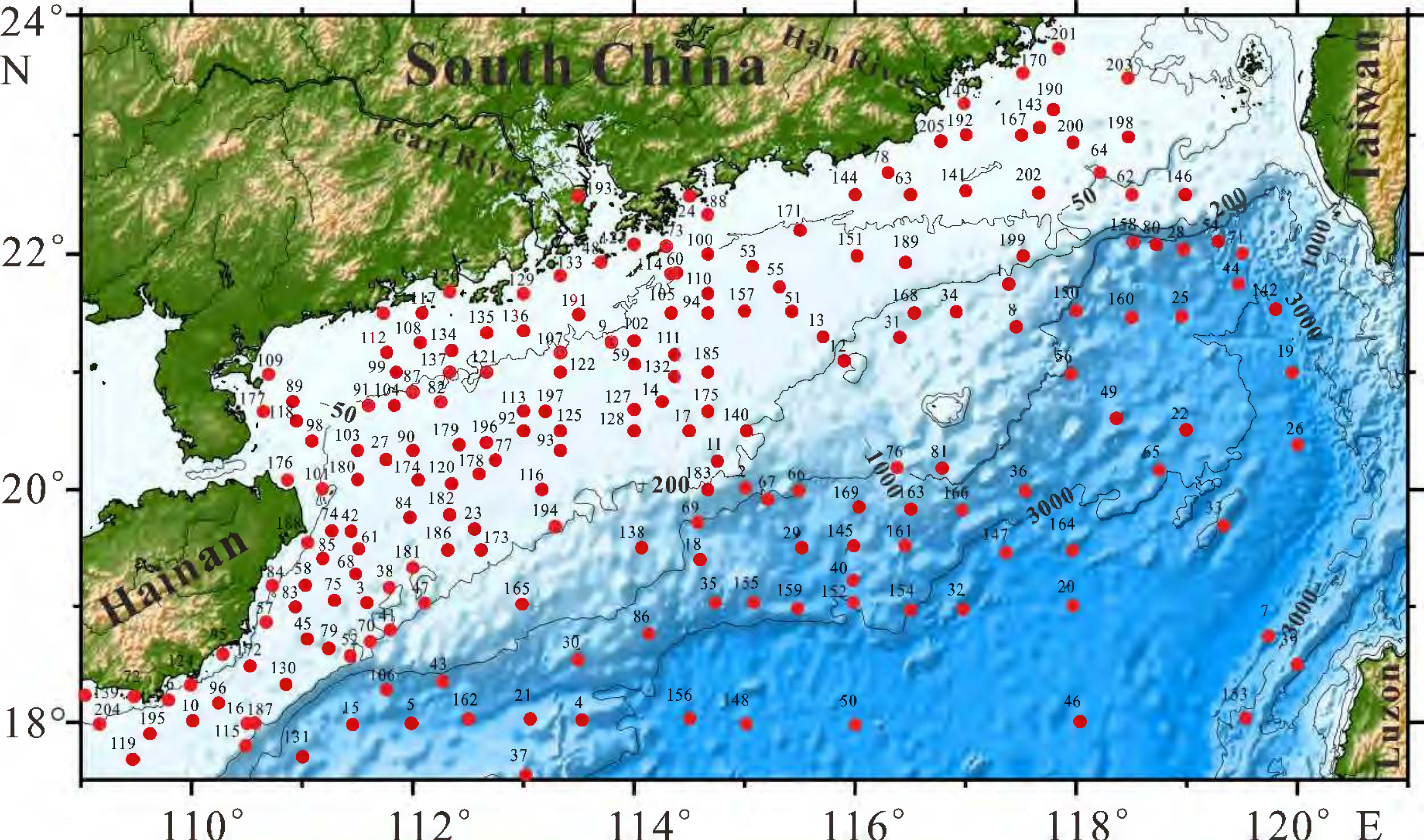
24° N
22°
20°
18°
110°
112°
114°
116°
118°
120° E
South China
Han River
Pearl River
Taiwan
Hainan
Luzon
50
200
1000
3000
201
170
203
149
190
143
192
167
200
198
205
78
64
144
63
141
202
62
146
193
188
24
171
158
80
28
54
71
151
189
199
48
123
73
100
53
114
60
55
133
110
1
44
105
94
157
51
168
34
150
160
25
142
117
129
191
13
8
31
135
136
108
112
134
107
9
102
111
185
12
56
19
121
99
87
137
59
132
122
109
89
91
104
82
127
14
175
49
177
118
113
197
125
22
98
92
128
17
140
26
196
103
27
90
179
93
77
76
81
65
176
11
101
180
174
120
178
116
36
183
2
67
66
169
163
166
84
182
69
3000
74
42
23
194
33
61
186
173
138
29
145
161
147
164
85
181
18
68
40
84
58
38
35
155
159
152
154
32
20
83
75
3
47
165
57
41
86
7
45
79
70
95
52
30
39
172
130
124
106
43
72
139
6
96
10
156
148
50
46
16
187
153
204
162
21
4
15
5
195
115
131
119
37

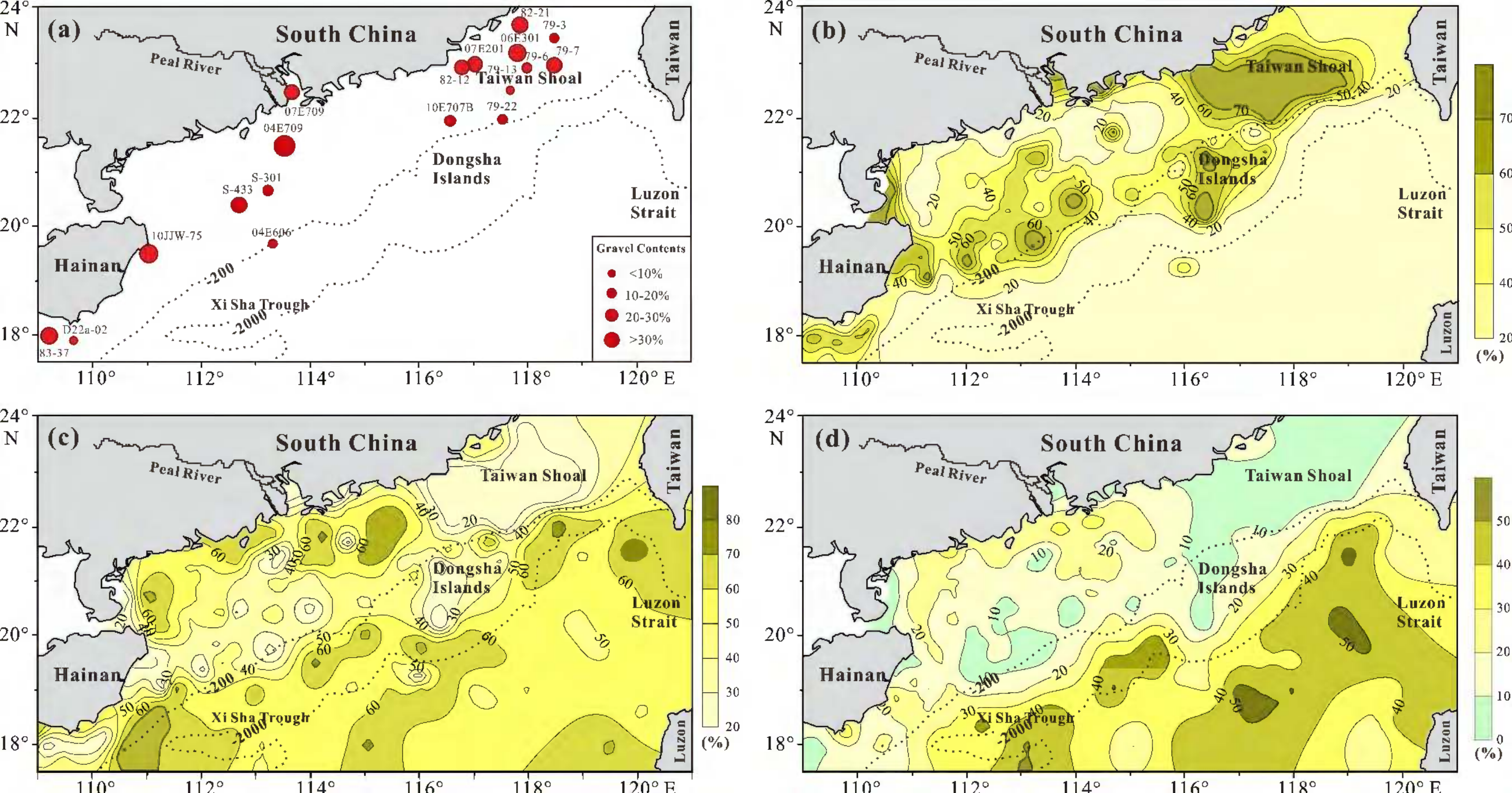
(a)
(b)
(c)
(d)
South China
Peal River
Taiwan Shoal
Taiwan
Dongsha Islands
Luzon Strait
Luzon
Hainan
Xi Sha Trough
-200
-2000
24° N
22°
20°
18°
110°
112°
114°
116°
118°
120° E
82-21
79-3
06E301
07E201
79-7
79-6
79-13
82-12
07E709
10E707B
79-22
04E709
S-301
S-433
10JJW-75
04E606
D22a-02
83-37
Gravel Contents
<10%
10-20%
20-30%
>30%
(%)
20
30
40
50
60
70
80
0
10

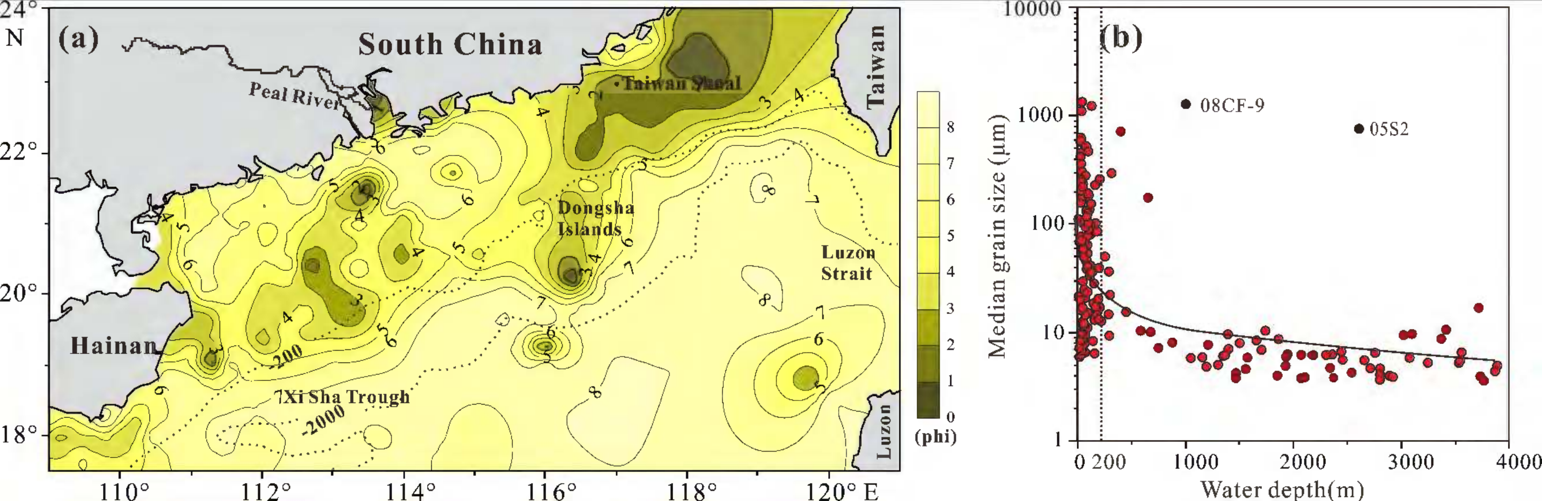
(a)
South China
Taiwan
Taiwan Shoal
Peal River
Dongsha Islands
Luzon Strait
Hainan
Xi Sha Trough
Luzon
-200
-2000
24° N
22°
20°
18°
110°
112°
114°
116°
118°
120° E
(phi)
0
1
2
3
4
5
6
7
8
(b)
08CF-9
05S2
Median grain size (μm)
Water depth(m)
10000
1000
100
10
1
0
200
1000
2000
3000
4000

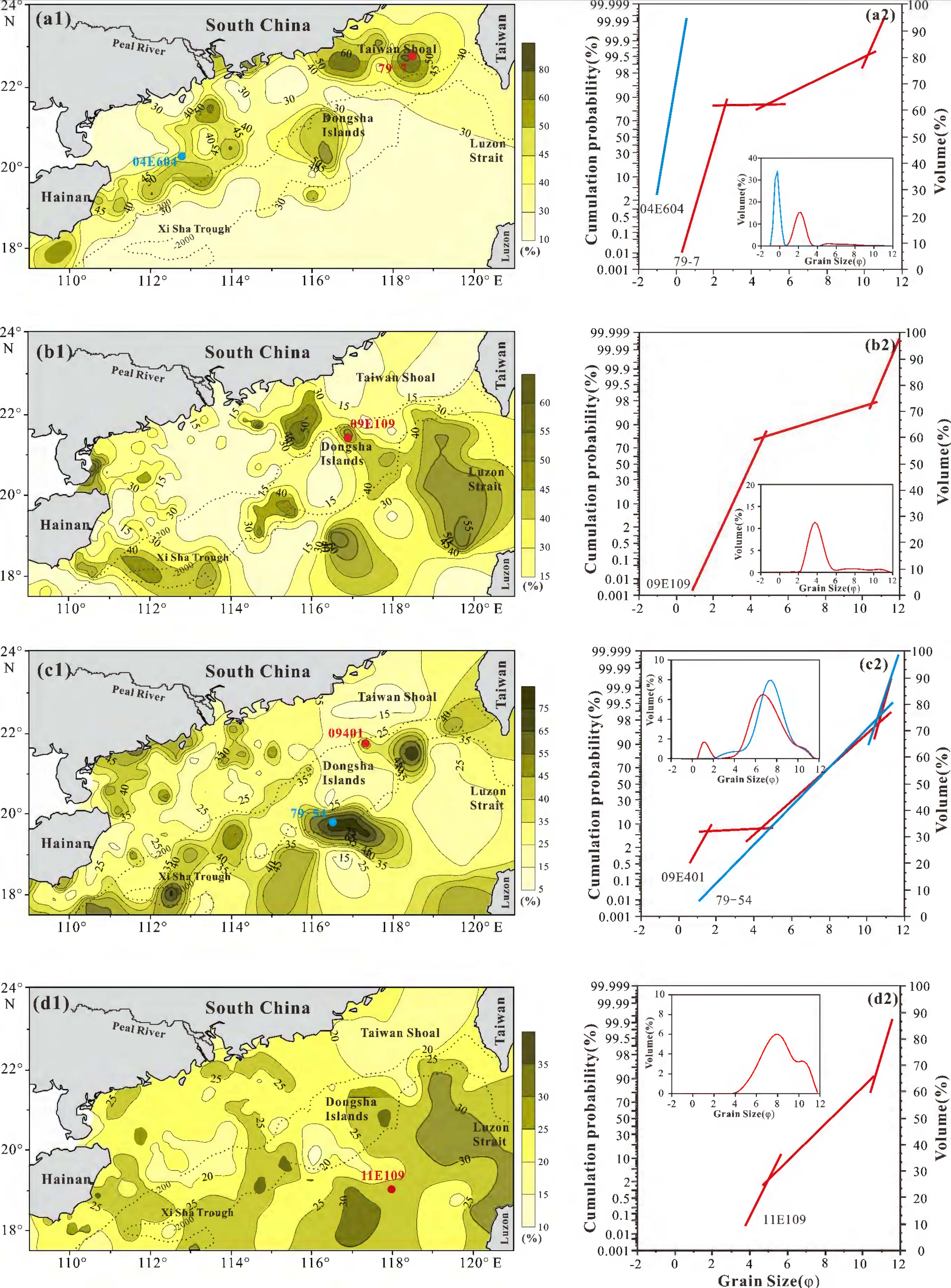
(a1)
South China
Peal River
Taiwan Shoal
Taiwan
Dongsha Islands
Luzon Strait
Hainan
Xi Sha Trough
Luzon
04E604
79-7
(%)
24° N
22°
20°
18°
110°
112°
114°
116°
118°
120° E
(a2)
Cumulation probability(%)
Volume(%)
Grain Size(φ)
04E604
79-7
(b1)
09E109
(b2)
09E109
(c1)
09401
79-54
(c2)
09E401
79-54
(d1)
11E109
(d2)
11E109
Grain Size(φ)

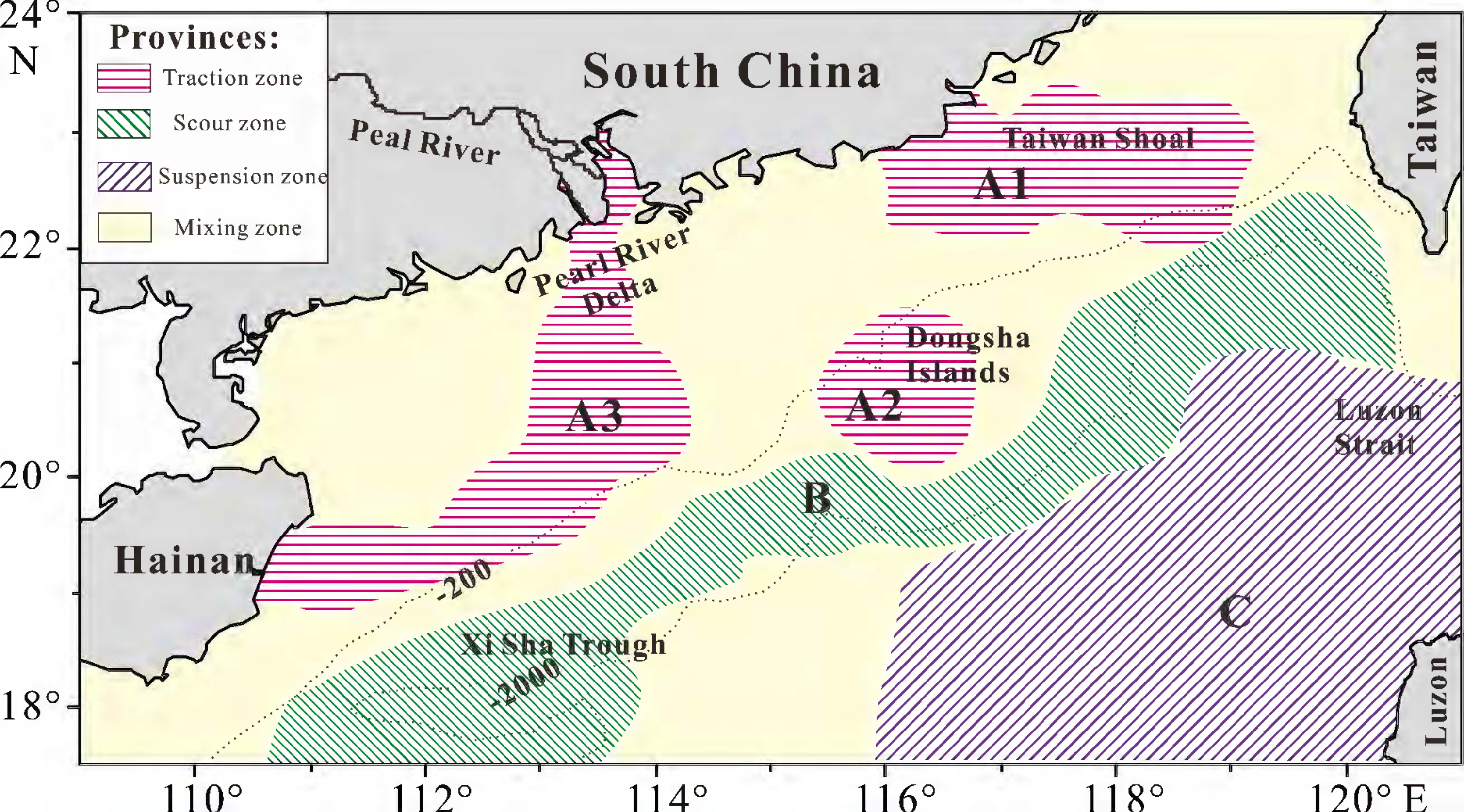
24° N
Provinces:
Traction zone
Scour zone
Suspension zone
Mixing zone
South China
Peal River
Taiwan Shoal
A1
Taiwan
22°
Pearl River Delta
Dongsha Islands
A3
A2
Luzon Strait
20°
B
Hainan
-200
C
Xi Sha Trough
-2000
18°
Luzon
110°
112°
114°
116°
118°
120° E

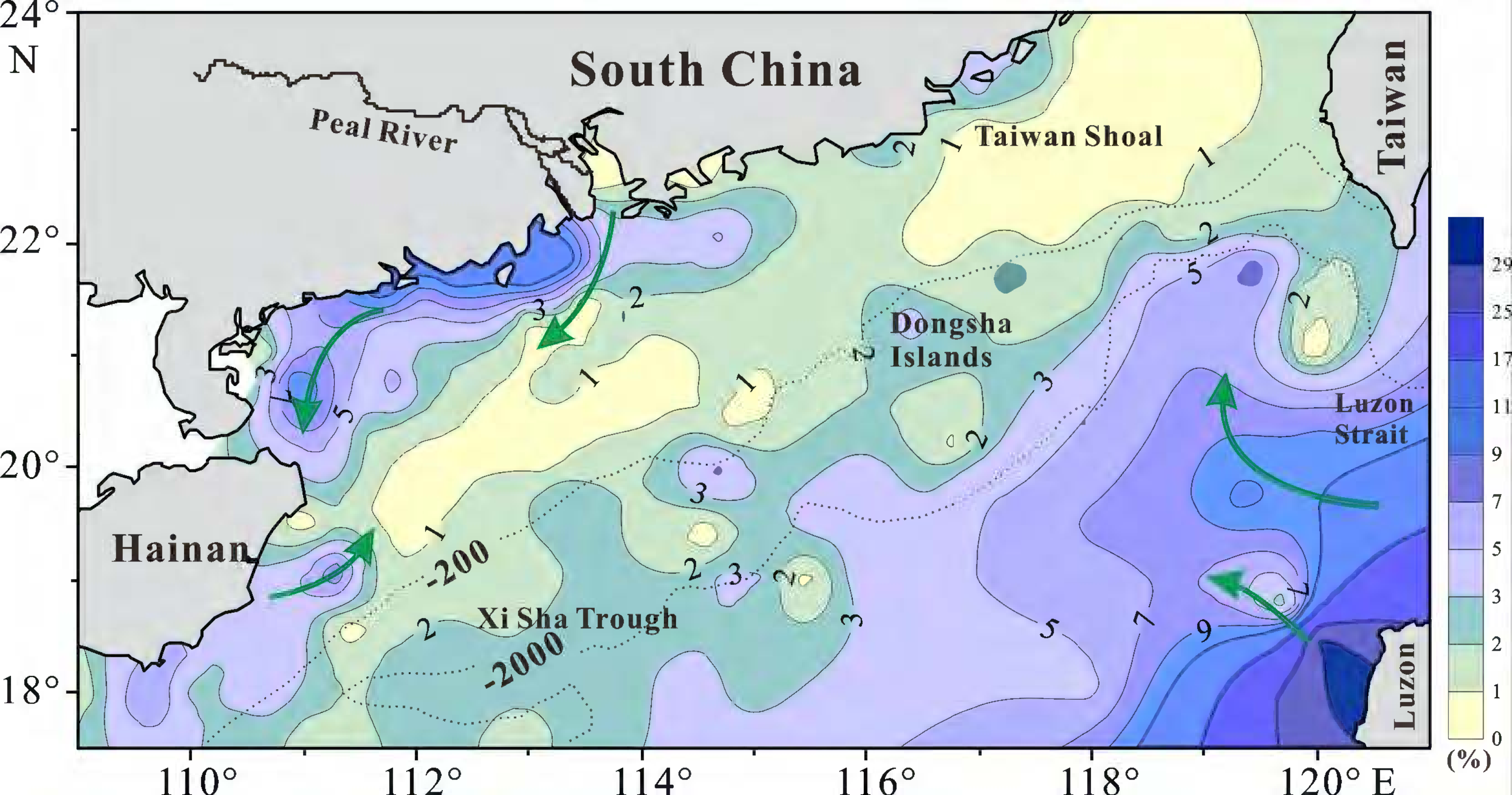
South China
Peal River
Taiwan Shoal
Taiwan
Dongsha Islands
Luzon Strait
Hainan
Xi Sha Trough
Luzon
-200
-2000
24° N
22°
20°
18°
110°
112°
114°
116°
118°
120° E
29
25
17
11
9
7
5
3
2
1
0
(%)

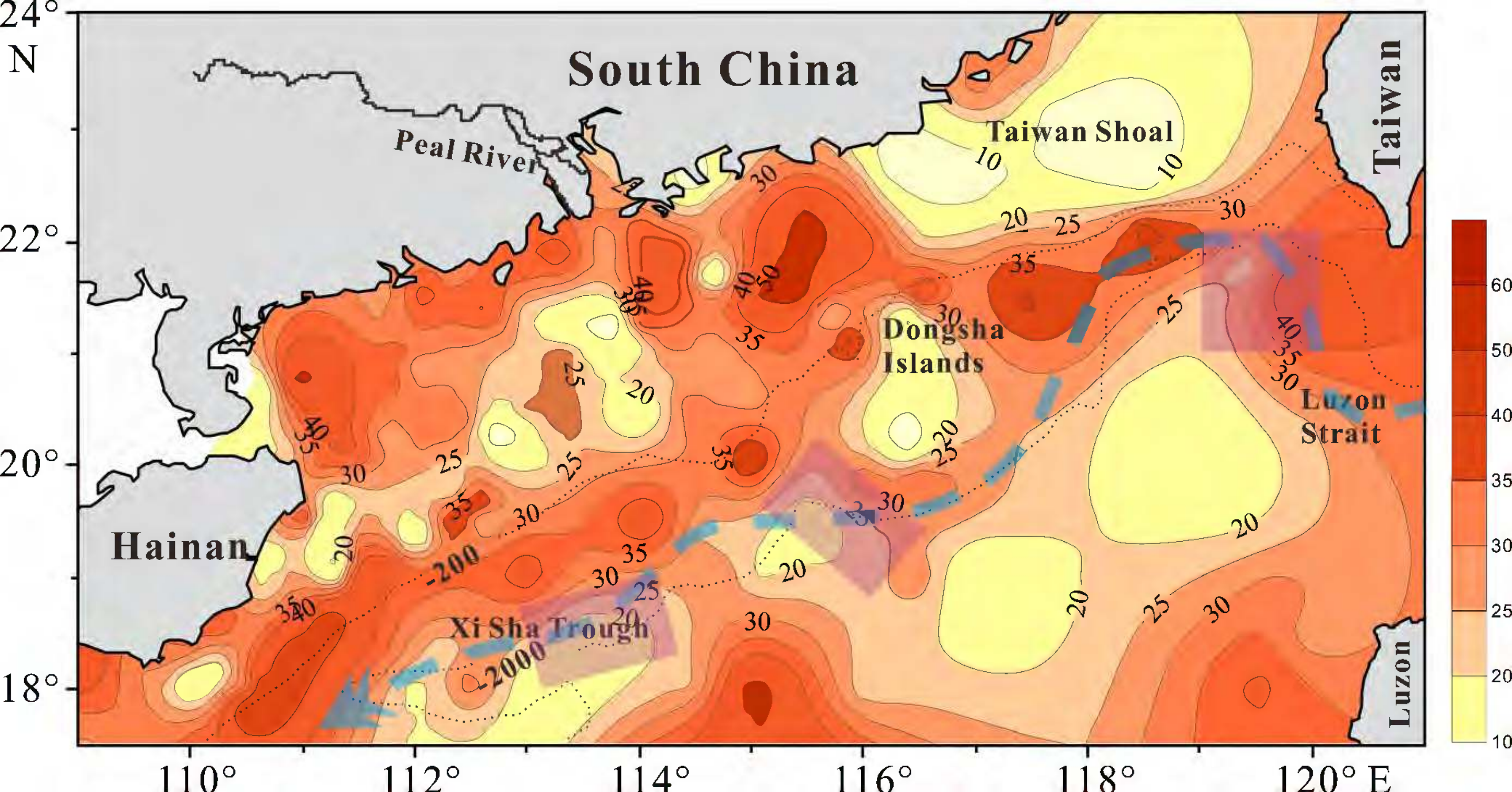
24° N
22°
20°
18°
110°
112°
114°
116°
118°
120° E
South China
Peal River
Taiwan Shoal
Taiwan
Dongsha Islands
Luzon Strait
Hainan
Xi Sha Trough
Luzon
-200
-2000
60
50
40
35
30
25
20
10

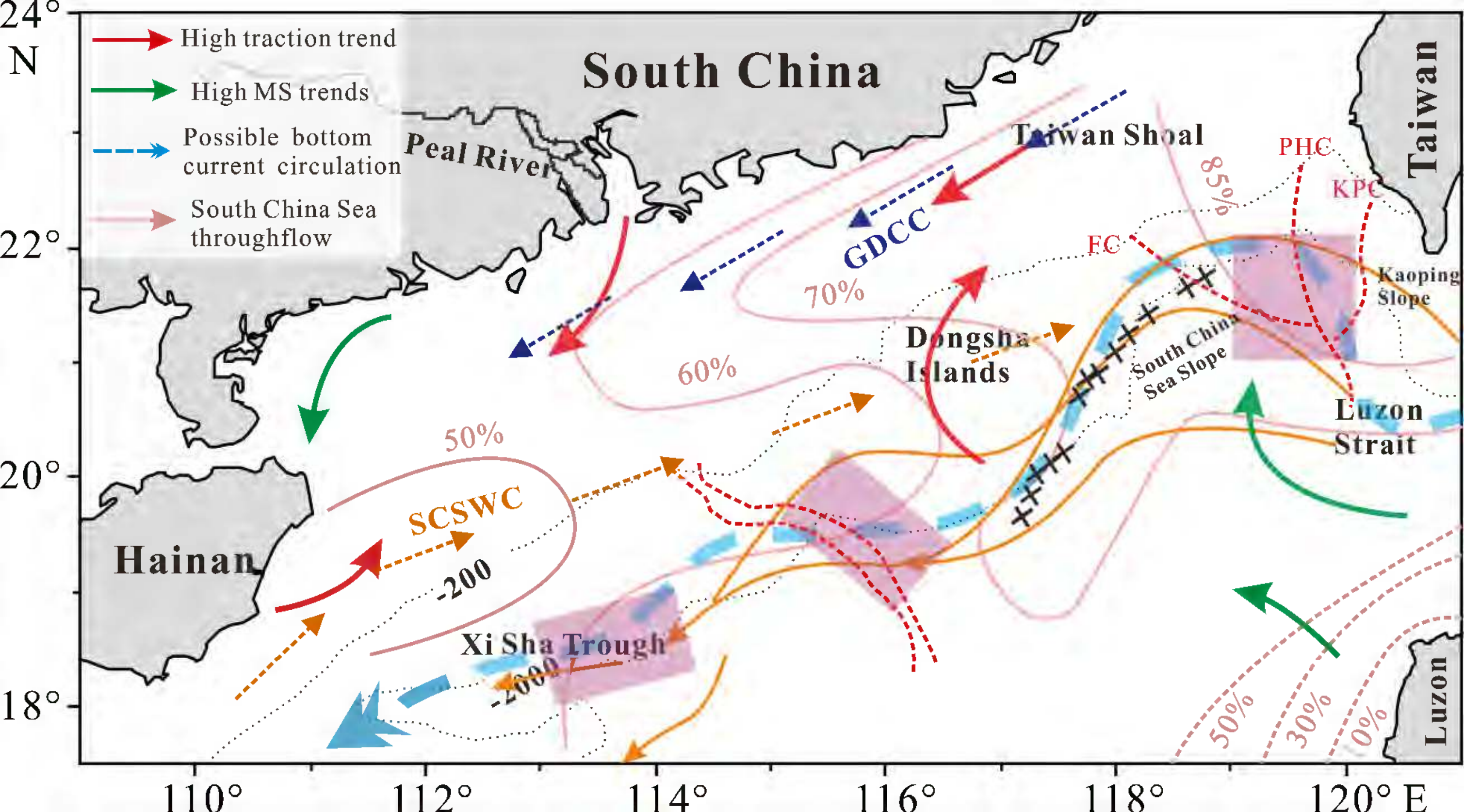
High traction trend
High MS trends
Possible bottom current circulation
South China Sea throughflow
South China
Taiwan
Peal River
Taiwan Shoal
GDCC
PHC
KPC
FC
85%
70%
60%
50%
Dongsha Islands
South China Sea Slope
Kaoping Slope
Luzon Strait
SCSWC
-200
-2000
Hainan
Xi Sha Trough
50%
30%
0%
Luzon
24°
N
22°
20°
18°
110°
112°
114°
116°
118°
120° E